SIAM J. Applied Dynamical Systems
Vol. 19, No. 1, pp. 442–479

Elliptic Bubbles in Moser's 4D Quadratic Map: The Quadfurcation*

Arnd Bäcker† and James D. Meiss‡

Abstract. Moser derived a normal form for the family of four-dimensional (4D), quadratic, symplectic maps in 1994. This six-parameter family generalizes Hénon's ubiquitous 2D map and provides a local approximation for the dynamics of more general 4D maps. We show that the bounded dynamics of Moser's family is organized by a codimension-three bifurcation that creates four fixed points—a bifurcation analogous to a doubled, saddle-center—which we call a *quadfurcation*. In some sectors of parameter space a quadfurcation creates four fixed points from none, and in others it is the collision of a pair of fixed points that re-emerge as two or possibly four. In the simplest case the dynamics is similar to the cross product of a pair of Hénon maps, but more typically the stability of the created fixed points does not have this simple form. Up to two of the fixed points can be doubly elliptic and surrounded by bubbles of invariant two-tori; these dominate the set of bounded orbits. The quadfurcation can also create one or two complex-unstable (Krein) fixed points. Special cases of the quadfurcation correspond to a pair of weakly coupled Hénon maps near their saddle-center bifurcations.

Key words. Hénon map, symplectic maps, saddle-center bifurcation, Krein bifurcation, invariant tori

AMS subject classifications. 37J10, 37J20, 37J25, 70K43

DOI. 10.1137/19M1268665

1. Introduction.

Multidimensional Hamiltonian systems model dynamics on scales ranging from zettameters, for the dynamics of stars in galaxies [1, 2], to nanometers, in atoms and molecules [3, 4]. Hamiltonian flows generate symplectic maps on Poincaré sections [5, sect. 9.14], and numerical algorithms for these flows can be symplectic [6, 7]. Symplectic maps also arise directly in discrete-time models of such phenomena as molecular vibrations [8, 9], stability of particle storage rings [10, 11], heating of particles in plasmas [12], microwave ionization of hydrogen [13], and chaos in celestial mechanics [14].

A map $f : \mathbb{R}^{2n} \to \mathbb{R}^{2n}$ is canonically symplectic for coordinates $x \in \mathbb{R}^n$ and momenta $y \in \mathbb{R}^n$ if its Jacobian matrix, $Df(x, y)$, satisfies

$$Df^T J Df = J, \quad J = \begin{pmatrix} 0 & -I \\ I & 0 \end{pmatrix}, \tag{1.1}$$

*Received by the editors June 14, 2019; accepted for publication (in revised form) by V. Rom-Kedar October 10, 2019; published electronically February 4, 2020.
https://doi.org/10.1137/19M1268665
Funding: This work was supported by the U. S. National Science Foundation under grants DMS-1440140 and DMS-181248, and by the Deutsche Forschungsgemeinschaft under grant KE 537/6-1. The second author was also supported as a Dresden Senior Fellow of the Technische Universität Dresden.
†Institut für Theoretische Physik and Center for Dynamics, Technische Universität Dresden, 01062 Dresden, Germany, and Max-Planck-Institut für Physik komplexer Systeme, 01187 Dresden, Germany (arnd.baecker@tu-dresden.de).
‡Department of Applied Mathematics, University of Colorado, Boulder, CO 80309-0526 (jdm@colorado.edu).

where J is the Poisson matrix. In particular, this implies that the map is volume preserving; i.e., $\det(Df) = 1$.

Perhaps the most famous symplectic map is the area-preserving map introduced by Hénon in 1969 as an elemental model to inform his studies of celestial mechanics [15]. This map is also the simplest nonlinear symplectic map, since it contains a single quadratic term, and yet—as Hénon showed—every quadratic area-preserving map can be reduced to his form [16].

Quadratic maps are useful because they model the dynamics of smooth maps in the neighborhood of a fixed point or that of a flow near a periodic orbit. For example, quadratic terms in the power series give a local description of the dynamics near an accelerator mode of Chirikov's standard map [17]. More generally, any symplectic diffeomorphism can be C^∞ approximated by a polynomial map on a compact set [18].

Higher-dimensional analogues of Hénon's map were proposed in [19], and similar maps were used to study the stickiness of regions near an elliptic fixed point [20], the resonant formation of periodic orbits and invariant circles [21, 22, 23, 24], bifurcations due to twist singularities [25], and the dynamics near a homoclinic orbit to a saddle-center fixed point [26]. Such maps model a focusing-defocusing (FODO) magnet cell in a particle accelerator and have been used to study the structure of bounded orbits, the dynamic aperture, and robustness of invariant tori [27, 28, 29, 30].

In 1994, Moser [31] showed that every quadratic symplectic map on $\mathbb{R}^{2n}$ is conjugate to the form

$$f = \alpha \circ \sigma \circ \beta. \tag{1.2}$$

Here $\alpha, \beta : \mathbb{R}^{2n} \to \mathbb{R}^{2n}$ are symplectic maps, β is linear, α is affine, and $\sigma : \mathbb{R}^n \times \mathbb{R}^n \to \mathbb{R}^n \times \mathbb{R}^n$ is a symplectic shear,

$$\sigma(x, y) = (x, y - \nabla V(x)), \tag{1.3}$$

where $V : \mathbb{R}^n \to \mathbb{R}$ is a cubic potential. There are several immediate consequences of this representation. First, if the quadratic map f has finitely many fixed points, as it generically will, then there are at most 2^n [31]. Note that, more generally, a quadratic nonsymplectic map on a $2n$-dimensional space could have as many as 2^{2n} isolated fixed points. Second, since the inverse of σ is also a quadratic shear of the same form (replace V by $-V$), the inverse of any quadratic, symplectic map is also quadratic. More generally, the inverse of a quadratic diffeomorphism could be a polynomial map of higher degree [32, Thm. 1.5]; for example, the inverse of the volume-preserving map $(x, y, z, w) \mapsto (x, y + x^2, z + y^2, w + z^2)$ has degree eight. The form (1.2) also applies to cubic maps but not to higher degree polynomial maps [33].

In this paper we study the dynamics of Moser's map in four dimensions. The normal form for the 4D case is reviewed and slightly transformed for convenience in section 2. We argue in section 3 that its fixed points are most properly viewed as arising from a bifurcation in which they emerge from a single fixed point as parameters are varied away from a codimension-three surface. Since this bifurcation often results in the creation of four fixed points, we call it a *quadfurcation*, with thanks to Strogatz, who, "with tongue in cheek," proposed the term in an exercise for 1D ODEs in his well-known textbook [34, Ex. 3.4.12].

As we will see in section 3.1, the unfolding of the quadfurcation in Moser's map can lead to (i) the creation of four fixed points from none, (ii) a collision and re-emergence of two pairs

of fixed points, or (iii) even the collision of a pair leading to four fixed points. The stability of these fixed points is investigated in section 3.2. The unfolding of the quadfurcation along paths in parameter space is studied in sections 3.3–3.4. When the map is reversible (see section 3.5), additional cases occur including the simplest one: the Cartesian product of a pair of area-preserving maps.

We numerically investigate the creation of families of invariant two-tori, as expected from Kolmogorov–Arnold–Moser (KAM) theory, around doubly elliptic fixed points in section 4. In section 5 we observe that these bubbles of elliptic orbits strongly correlate with the regions of bounded dynamics.

Since Moser's map is affinely conjugate to the general quadratic, symplectic map, it must have a limit in which it reduces to a pair of uncoupled Hénon maps—we show this in section 6.

2. Moser's quadratic, symplectic map.

2.1. Four-dimensional normal form. For the two-dimensional case, the map (1.2) can be generically transformed by an affine coordinate change to the Hénon map H,

$$H(x,y) = (-y + a_{\mathrm{h}} + x^2, x), \tag{2.1}$$

with a single parameter a_{h}. When this map has an elliptic fixed point (for $-3 < a_{\mathrm{h}} < 1$), it is conjugate to the map whose dynamics were first studied by Hénon [15]. By a similar transformation, Moser showed [31] that in four dimensions, (1.2) can be generically written as

$$(x', y') = f(x,y) = (C^{-T}(-y + \nabla V(x)), Cx), \tag{2.2}$$

where

$$\begin{aligned} C &= \begin{pmatrix} \alpha & \beta \\ \gamma & \delta \end{pmatrix}, \\ V &= A_1 x_1 + A_2 x_2 + \frac{1}{2} A_3 x_1^2 + \varepsilon_2 x_1^3 + x_1 x_2^2, \end{aligned} \tag{2.3}$$

and $x \equiv (x_1, x_2) \in \mathbb{R}^2$, $y \equiv (y_1, y_2) \in \mathbb{R}^2$. Here there are two discrete parameters, $\varepsilon_1 \equiv \det(C) = \alpha\delta - \beta\gamma = \pm 1$ and $\varepsilon_2 \equiv \pm 1$ or 0. The remaining six parameters are free. We will refer to (2.2) as *Moser's map* below. It is convenient to think of the six real parameters of f as (A_1, A_2, A_3) and (α, δ, μ), where

$$\mu = \beta + \gamma. \tag{2.4}$$

Indeed, given these six, and the sign ε_1, we can determine the off-diagonal elements of C from

$$\beta, \gamma = \frac{1}{2}\mu \pm \sqrt{\varepsilon_1 - \alpha\delta + \mu^2/4}. \tag{2.5}$$

The choice of the sign here is unimportant since this simply replaces C with C^T, and the resulting map is conjugate to the inverse of (2.2); see section 2.3. Note that (2.5) has real solutions only when $\mu^2 \geq 4(\alpha\delta - \varepsilon_1)$ and that C is symmetric only at the lower bound of this inequality.

The map (2.2) is easily seen to be symplectic (1.1) as it is the composition of the symplectic shear (1.3), the Poisson map, $J(x, y) = (-y, x)$, and the linear symplectic map,

$$(x, y) \mapsto (C^{-T}x, Cy).$$

2.2. Shifted coordinates. As a first step in the analysis of the dynamics of (2.2), we will study its fixed points. To do this it is convenient to define shifted variables and parameters. There is a codimension-three set of parameters where the map has exactly one fixed point, and focusing on this set simplifies the calculations more generally.

For any matrix C and when $\varepsilon_2 \neq 0$, the map (2.2) has exactly one fixed point at

$$\begin{aligned} x^{\mathrm{Q}} &= (\delta, \tfrac{1}{2}\mu), \\ y^{\mathrm{Q}} &= Cx^{\mathrm{Q}}, \end{aligned} \tag{2.6}$$

when the parameters (A_1, A_2, A_3) of the potential (2.3) take the values

$$\begin{aligned} A_1^{\mathrm{Q}} &= 3\delta^2\varepsilon_2 + \frac{1}{4}\mu^2, \\ A_2^{\mathrm{Q}} &= \delta\mu, \\ A_3^{\mathrm{Q}} &= 2\alpha - 6\delta\varepsilon_2. \end{aligned} \tag{2.7}$$

To see this, and to simplify the computations, it is convenient to shift coordinates, so that the origin is at the point $(x^{\mathrm{Q}}, y^{\mathrm{Q}})$, and to define the following new shifted parameters:

$$\begin{aligned} (\xi, \eta) &= (x - x^{\mathrm{Q}}, y - y^{\mathrm{Q}}), \\ a &= A_1 - A_1^{\mathrm{Q}} + \delta(A_3 - A_3^{\mathrm{Q}}), \\ b &= A_2 - A_2^{\mathrm{Q}}, \\ c &= A_3 - A_3^{\mathrm{Q}}. \end{aligned} \tag{2.8}$$

In these new coordinates, (2.2) becomes

$$(\xi', \eta') = M(\xi, \eta) = (\xi + C^{-T}(-\eta + C\xi + \nabla U(\xi)), C\xi), \tag{2.9}$$

where the new potential,

$$U = a\xi_1 + b\xi_2 + \frac{1}{2}c\xi_1^2 + \varepsilon_2\xi_1^3 + \xi_1\xi_2^2, \tag{2.10}$$

is the same as V from (2.3) upon replacing (A_1, A_2, A_3) by (a, b, c). This shifted form of Moser's quadratic, symplectic map is convenient because several computations can be carried out more easily, and many of the expressions we obtain below will be more compact.

The map (2.9) is generated by the discrete Lagrangian,

$$\mathcal{L}(\xi, \xi') = (\xi' - \xi)^T C\xi - U(\xi), \tag{2.11}$$

through the equation

$$\eta' d\xi' - \eta d\xi = d\mathcal{L}(\xi, \xi').$$

In other words, the map is implicitly defined by $\eta = -\partial_\xi \mathcal{L}(\xi, \xi')$ and $\eta' = \partial_{\xi'} \mathcal{L}(\xi, \xi')$. This means that M is *exact* symplectic [35] and, of course, that it preserves the symplectic form $d\xi \wedge d\eta$. Note also that if we denote an orbit of (2.9) as a sequence

$$\{(\xi_t, \eta_t) \in \mathbb{R}^4 \,|\, (\xi_t, \eta_t) = M(\xi_{t-1}, \eta_{t-1}),\, t \in \mathbb{Z}\} \tag{2.12}$$

and define the action of a finite portion by

$$\mathcal{A} = \sum_{t=j}^{k-1} \mathcal{L}(\xi_t, \xi_{t+1}),$$

then each stationary point of $\mathcal{A}$, for fixed endpoints, is a segment of an orbit with the momentum determined by $\eta_{t+1} = C\xi_t$.

2.3. Second difference form and ODE limit. The shifted form (2.9) of Moser's map (2.2) can be written as a second difference equation. If we denote an orbit as (2.12), then $\eta_t = C\xi_{t-1}$, and the map (2.9) is equivalent to

$$C^T(\xi_{t+1} - \xi_t) - C(\xi_t - \xi_{t-1}) = \nabla U(\xi_t). \tag{2.13}$$

One immediate consequence of (2.13) is that the replacement $C \to C^T$ is clearly equivalent to inverting the map. Therefore the invariant sets of the Moser map with $C \to C^T$ are the same as those of the original map. Similarly, note that the replacement $C \to -C$, together with $\xi \to -\xi$ and $c \to -c$, leaves the Moser map invariant. We will also use the form (2.13) in sections 3.2 and 5.

To emphasize the different roles of the symmetric and antisymmetric parts of C, let

$$\begin{aligned} C &= C^{\mathrm{s}} + C^{\mathrm{a}}, \\ C^{\mathrm{s}} &\equiv \frac{1}{2}(C + C^T) = \begin{pmatrix} \alpha & \mu/2 \\ \mu/2 & \delta \end{pmatrix}, \\ C^{\mathrm{a}} &\equiv \frac{1}{2}(C - C^T) = \begin{pmatrix} 0 & \nu/2 \\ -\nu/2 & 0 \end{pmatrix}, \end{aligned} \tag{2.14}$$

where $\nu = \beta - \gamma$ and, as before, $\mu = \beta + \gamma$. Then (2.13) becomes

$$C^{\mathrm{s}}(\xi_{t+1} - 2\xi_t + \xi_{t-1}) - C^{\mathrm{a}}(\xi_{t+1} - \xi_{t-1}) = \nabla U(\xi_t). \tag{2.15}$$

In this form the map closely resembles a pair of second-order differential equations.

Indeed, in a neighborhood of the origin in the phase space, (ξ, η), and in the space of the new parameters, (a, b, c, ν), (2.15) approaches a Lagrangian system of ODEs. To see this, formally introduce a parameter h, and scale

$$(a, b, c, \nu) \to (h^4 a, h^4 b, h^2 c, h\nu).$$

Here $h\nu$ represents the deviation from symmetry, so that $C \to C^{\mathrm{s}} + hC^{\mathrm{a}}$. Then in the limit $h \to 0$, the second difference equation (2.13) limits on a system of ODEs in a scaled time, $\tau = ht$, and a new variable

$$\xi_t \to h^2 q(\tau).$$

This scaling implies that for the potential (2.10), $\nabla_\xi U(\xi) \to h^4 \nabla_q U(q)$. Moreover, as $h \to 0$, the second difference $\xi_{t+1} - 2\xi_t + \xi_{t-1} \to h^4 \ddot{q}(\tau) + \mathcal{O}(h^5)$, and the first difference $\xi_{t+1} - \xi_{t-1} \to 2h^3 \dot{q}(\tau) + \mathcal{O}(h^4)$. Substituting these into (2.15) gives the limiting system

$$C^{\mathrm{s}} \ddot{q} - 2C^{\mathrm{a}} \dot{q} = \nabla U(q), \tag{2.16}$$

as $h \to 0$. Thus the symmetric part of C corresponds to a mass matrix, multiplying the acceleration. In contrast, C^{a} corresponds to a Coriolis-like force, which is proportional to the velocity.

The system (2.16) is obtained from the Lagrangian

$$L(q, \dot{q}) = \frac{1}{2} \dot{q}^T C^{\mathrm{s}} \dot{q} + q^T C^{\mathrm{a}} \dot{q} + U(q). \tag{2.17}$$

To convert (2.16) into a Hamiltonian system, define the canonical momenta

$$p(\tau) = \frac{\partial L}{\partial \dot{q}} = C^{\mathrm{s}} \dot{q} - C^{\mathrm{a}} q,$$

giving a Hamiltonian, $H = p\dot{q} - L$, that has Coriolis and centripetal terms as follows:

$$H(q, p) = \frac{1}{2} p^T C^{\mathrm{s}} p + p^T C^{\mathrm{s}} C^{\mathrm{a}} q - \frac{1}{2} q^T (C^{\mathrm{a}} C^{\mathrm{s}} C^{\mathrm{a}}) q - U(q). \tag{2.18}$$

Thus C^{s} is the mass matrix, and U is the *negative* of the potential energy. The antisymmetric matrix C^{a} contributes both a Coriolis-like term, bilinear in q and p, and a centripetal-like term, quadratic in q. We will use this interpretation, for the case of symmetric C, in section 3.5.

3. Quadfurcation. From the general theory [31] we know that Moser's map (2.2), and hence (2.9), has at most four (isolated) fixed points. On the codimension-three surface $a = b = c = 0$ in parameter space there is a single fixed point (unless $\varepsilon_2 = 0$). As we will see below, there are sectors in parameter space near this surface for which there are no fixed points, and sectors for which there are four. It seems appropriate to call the creation of four fixed points from none a *quadfurcation*. In some cases a quadfurcation can be analogous to a simultaneous pair of colocated saddle-center bifurcations; however, the stabilities of the resulting fixed points are usually not those of a pair of decoupled area-preserving maps, namely the Cartesian product of 2D saddles and centers.

In the following subsections we study the fixed points, their stability, and the structure of the region of phase space around the elliptic fixed points that contains bounded orbits.

3.1. Fixed points. The coordinates, ξ^*, of the fixed points of (2.9) are critical points of the cubic polynomial (2.10). Several contour plots of $U(\xi)$ are shown in Figure 1. Critical points satisfy the equations

$$0 = \nabla U(\xi^*) = \begin{pmatrix} a + c\xi_1^* + 3\varepsilon_2 \xi_1^{*2} + \xi_2^{*2} \\ b + 2\xi_1^* \xi_2^* \end{pmatrix}. \tag{3.1}$$

Note that the positions are independent of the matrix C, though the momenta, determined by $\eta^* = C\xi^*$, depend on the full matrix. Note that if $\nabla U(\xi^*) = 0$ for parameters (a, b, c),

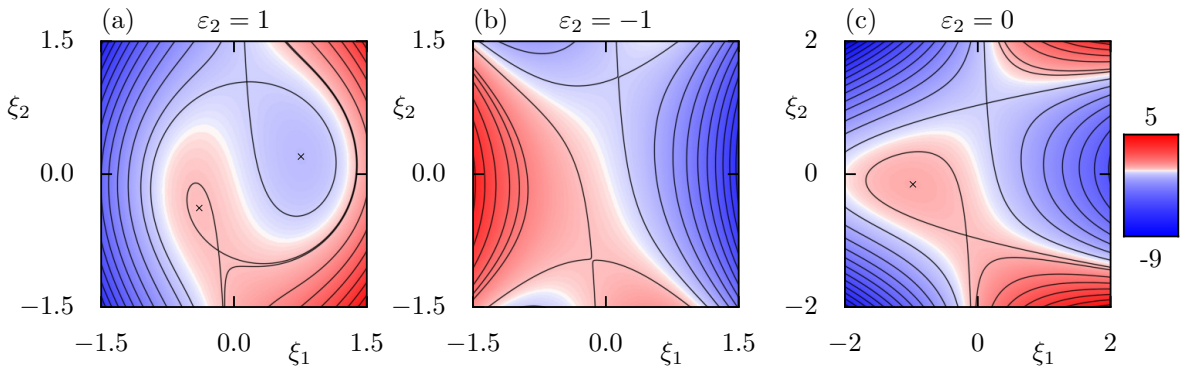

Figure 1. *Contour plots of the potential U (2.10) for $(a, b, c) = (-1, -0.3, -1)$. (a) $\varepsilon_2 = 1$. Here there are four critical points, implying four fixed points of (2.9). (b) $\varepsilon_2 = -1$, two critical points. (c) $\varepsilon_2 = 0$, three critical points.*

then it is also zero at the point $-\xi^*$ for parameters $(a, b, -c)$ and at the point $(\xi_1^*, -\xi_2^*)$ for $(a, -b, c)$. Thus we can restrict our attention to $b, c \geq 0$.

The case $a = b = c = 0$ is an organizing center for the solutions of (3.1). In this case the second component immediately implies that either $\xi_1^* = 0$ or $\xi_2^* = 0$. Then, whenever $\varepsilon_2 \neq 0$, the first implies that both $\xi_1^* = \xi_2^* = 0$. We call this the *quadfurcation point*. Since the matrix elements (α, δ, μ) are still free parameters, this point occurs on a codimension-three surface in the six-dimensional parameter space. The off-diagonal elements of the matrix, β and γ, are then fixed—up to exchange—by the condition $\det(C) = \varepsilon_1$, (2.5). In the parameterization (2.9) the quadfurcation surface is just the three-plane $a = b = c = 0$. In Moser's original parameterization, this surface is determined by (2.7).

More generally if $b \neq 0$, then (3.1) implies that $\xi_1^* \neq 0$, so

$$\xi_2^* = -\frac{b}{2\xi_1^*}. \tag{3.2}$$

Substituting into the first component of (3.1) then shows that ξ_1^* must be a root of the scalar polynomial

$$P(v; a, b, c, \varepsilon_2) = 3\varepsilon_2 v^4 + cv^3 + av^2 + \frac{1}{4}b^2. \tag{3.3}$$

When $\varepsilon_2 \neq 0$ this polynomial is quartic, and so it has at most four roots. Since P has no linear term, it has exactly one root in $\mathbb{C}$ on the quadfurcation set only when $a = b = c = 0$. When $\varepsilon_2 = 0$, $P(v)$ is at most cubic, and there are at most three isolated roots. Several examples are shown in Figure 2.

There are various regions in the parameter space (a, b, c) that have different numbers of fixed points. We now determine the bifurcation sets that separate these regions. To find these sets when $\varepsilon_2 \neq 0$, it is easiest to solve for the surfaces on which there are double roots, i.e., $P(v) = 0$ and $P'(v) = 0$. First, P always has a critical point, $P'(v) = 0$, at $v = 0$, and it has two more critical points if

$$\varepsilon_2 a < a_+(c) \equiv \frac{3}{32}c^2. \tag{3.4}$$

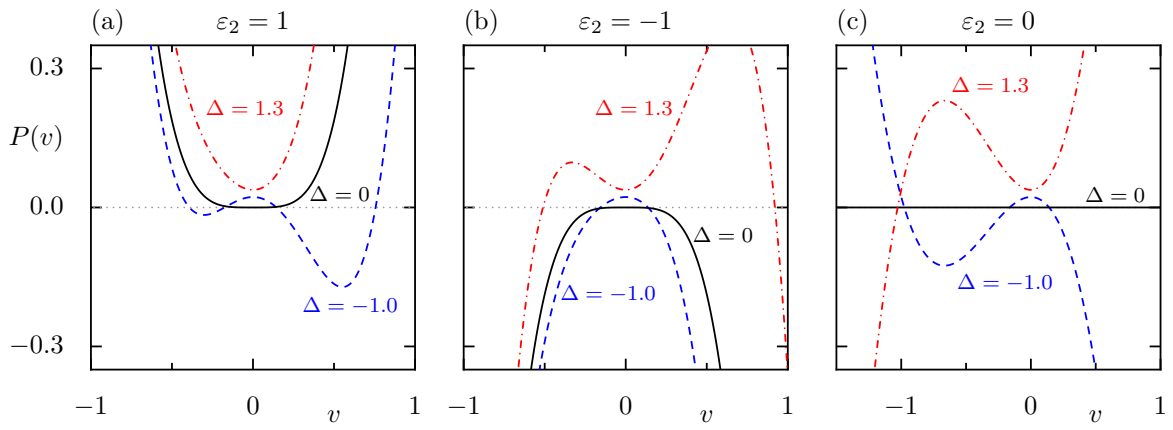

Figure 2. *The polynomial* $P(v)$ (3.3) *along the curve* $(a, b, c) = \Delta(1, 0.3, 1)$ *as* Δ *varies.* (a) $\varepsilon_2 = 1$, *where four roots are created when* Δ *decreases through zero;* (b) $\varepsilon_2 = -1$, *where there are two roots for any* $\Delta \neq 0$*;* *and* (c) $\varepsilon_2 = 0$ *with one root for* $\Delta > 0$, *infinitely many at* $\Delta = 0$, *and three for* $\Delta < 0$.

Eliminating v from the two equations $P(v) = P'(v) = 0$ gives the discriminant

$$b^2 \left[1728\varepsilon_2 b^4 + 9(-3c^4 + 48\varepsilon_2 ac^2 - 128a^2)b^2 - 16a^3c^2 + 192\varepsilon_2 a^4\right] = 0.$$

Thus there are double roots at $b = 0$, and on the surfaces $b = \pm\sqrt{D_\pm(a, c)}$, where

$$D_\pm(a, c) = \frac{\varepsilon_2}{384}\left(3(c^2 - 8\varepsilon_2 a)^2 - 64a^2 \pm \frac{|c|}{\sqrt{3}}(3c^2 - 32\varepsilon_2 a)^{3/2}\right). \tag{3.5}$$

For these surfaces to be real, the radical in (3.5) must be real, i.e., (3.4) must be satisfied. Moreover, if we let

$$a_-(c) \equiv \frac{1}{12}c^2, \tag{3.6}$$

then $D_+(\varepsilon_2 a_-, c) = 0$ and $D_-(0, c) = 0$. To define real-valued functions, let

$$\begin{aligned} b_+(a, c) &= \begin{cases} \sqrt{D_+(a, c)}, & a < \varepsilon_2 a_-, \text{ and } \varepsilon_2 a < a_+, \\ 0 & \text{otherwise,} \end{cases} \\ b_-(a, c) &= \begin{cases} \sqrt{D_-(a, c)}, & a < 0, \text{ and } \varepsilon_2 a < a_+, \\ 0 & \text{otherwise.} \end{cases} \end{aligned} \tag{3.7}$$

The resulting surfaces are shown in Figure 3.

If $\varepsilon_2 = 1$, then when $b > b_+$ there are no real roots. At the upper surface, $b = b_+(a, c)$, which is nonzero for $a < a_-$, two roots are created. Two additional roots are created upon crossing $b_-(a, c)$, which is nonzero for $a < 0$; see Table 1. The two surfaces $b_\pm(a, c)$ intersect at $c = 0$ on the line $a = -\sqrt{3}|b|$. Crossing this codimension-two set $b_- = b_+$ at $c = 0$ and moving into the region $b < b_-$ thus corresponds to the simultaneous creation of four fixed points at two different locations, i.e., to a pair of simultaneous saddle-center bifurcations, as we will see in section 3.2.

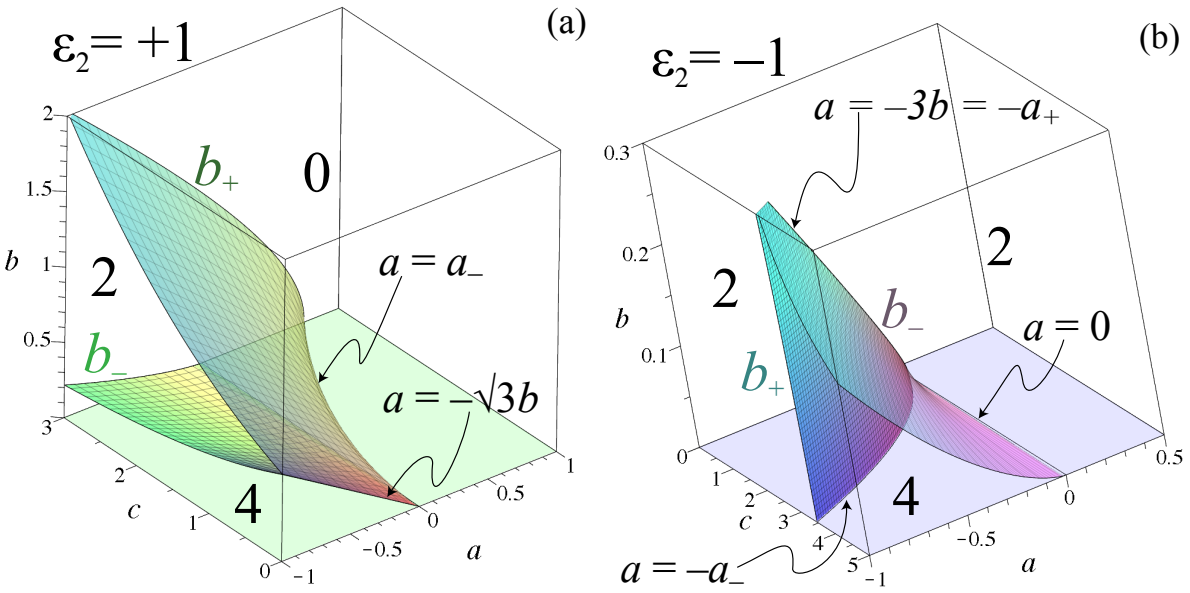

Figure 3. *Surfaces in (a, b, c) for which there are double roots of P (3.3) (a) when $\varepsilon_2 = 1$ and (b) when $\varepsilon_2 = -1$. For $\varepsilon_2 = 1$, when b is sufficiently positive, there are no real solutions; as b decreases through the b_+ surface (3.7), two solutions are created; and finally, when it passes through the b_- surface, there are four solutions. For $\varepsilon_2 = -1$, there are two solutions if b is sufficiently large. An additional two solutions are created upon moving through either of the $b_\pm$ surfaces. Curves where bifurcation surfaces intersect are also shown in each panel:* (a) *$a = a_-(c)$ on the $b = 0$ plane and $a - \sqrt{3}b$ on the $c = 0$ plane.* (b) *$a = 0$ and $-a_-(c)$ at $b = 0$ and $a = -3b = -a_+(c)$.*

If $\varepsilon_2 = -1$, then (3.3) has four real roots only if $-a_+ < a < 0$ and $b_+ < b < b_-$. Note that b_+ is nonzero only when $-a_- < a < 0$. Inside the cusp-like shape formed from the $b_\pm$ surfaces, as shown in Figure 3(b), there are four roots. Going outward from this region, by crossing either b_- or b_+, two solutions disappear in a saddle-center bifurcation. Thus on the surfaces $b = b_+$ or $b = b_-$ there are three roots (one of them with multiplicity 2). When these surfaces merge, on the curve $a = -a_+$ and $b = b_\pm(-a_+, c) = c^2/32$, there are two fixed points:

$$(\xi_1^*, \xi_2^*) = \begin{cases} \frac{c}{8}(1,-1) & \text{(multiplicity 3)} \\ \frac{c}{24}(-1,9) & \text{(multiplicity 1)} \end{cases} \qquad (\varepsilon_2 = -1, a = -3b = -a_+).$$

The cases $b = 0$ and $c = 0$ require special treatment. When $c = 0$ but $b \neq 0$, the polynomial (3.3) has no cubic term, and the fixed points can be solved for explicitly as follows:

$$\xi_1^* = \pm\sqrt{-\frac{1}{6}\varepsilon_2\left(a \pm \sqrt{a^2 - 3\varepsilon_2 b^2}\right)} \qquad (c = 0), \tag{3.8}$$

where ξ_2^* is then obtained from (3.2). Note that there are four possible points here, with choices for the outer $\pm$ and the inner $\pm$. This equation gives real solutions only when both square roots are real. When $\varepsilon_2 = 1$, (3.8) gives four real solutions if $a < -\sqrt{3}|b|$. On the boundary $a = -\sqrt{3}|b|$, these four solutions are created in two pairs at

$$(\xi_1^*, \xi_2^*) = \pm\sqrt{-\frac{a}{6}}\left(1, -\sqrt{3}\,\mathrm{sgn}(b)\right) \qquad (\varepsilon_2 = 1, a = -\sqrt{3}|b|, c = 0).$$

Table 1

Number of fixed points of the map (2.9) depending upon ε_2 and parameters (a, b, c). Since this number is an even function of b and c, we can assume that both are nonnegative. The functions $b_\pm(a, c)$ are given by (3.7), and $a_\pm(c)$ are given by (3.4) and (3.6). The additional three rows in each ε_2 section delineate special cases when either b or c is zero or both are zero.

			Number of fixed points				
ε_2	b	c	0	1	2	3	4
1			$b > b_+$	$b = b_+$	$b \in (b_-, b_+)$	$b = b_-$	$b < b_-$
	0		$a > a_-$	$a = a_-$	$0 < a < a_-$	$a = 0$	$a < 0$
		0	$a > -\sqrt{3}\lvert b\rvert$		$a = -\sqrt{3}\lvert b\rvert$		$a < -\sqrt{3}\lvert b\rvert$
	0	0	$a > 0$	$a = 0$			$a < 0$
-1					$a \notin (-a_+, 0]$ or $b \notin [b_+, b_-]$	$b = b_+$, or $b = b_-$	$a \in (-a_+, 0)$ and $b \in (b_+, b_-)$
	0				$a \notin [-a_-, 0]$	$a = -a_-, 0$	$a \in (-a_-, 0)$
		0			always		
	0	0		$a = 0$	$a \neq 0$		
0				$a > -a_0$	$a = -a_0$	$a < -a_0$	
	0			$a > 0$	$a = 0$	$a < 0$	
		0	$a \geq 0$		$a < 0$		
	0	0	$a > 0$		$a < 0$		

These pairs merge at the quadfurcation point $a = b = c = 0$. If $\varepsilon_2 = -1$, then only the inner $+$ sign choice is valid, and (3.8) gives two real solutions whenever a or $b \neq 0$. Table 1 delineates the possibilities.

If $b = 0$, then (3.1) implies that either $\xi_1^* = 0$ or $\xi_2^* = 0$. The first component of (3.1) is then trivially a quadratic function. In this case the four solutions are

$$(\xi_1^*, \xi_2^*) = \begin{cases} \left(0, \pm\sqrt{-a}\right) \\ \left(\frac{\varepsilon_2}{6}(-c \pm \sqrt{c^2 - 12\varepsilon_2 a}), 0\right) \end{cases} \qquad (b = 0). \tag{3.9}$$

Note that when $\varepsilon_2 = 1$, there are four real fixed points whenever $a < 0$, and there are two in the range $0 < a < a_-$. If $\varepsilon_2 = -1$, then the first pair is real when $a \leq 0$, and the second pair is real only if $a \geq -a_-$. Thus there are four real fixed points when $-a_- < a < 0$.

For $\varepsilon_2 = 0$ and $c \neq 0$, the polynomial (3.3) is cubic, so there is always at least one fixed point. The critical points of P are at $v = 0$ and $v = -2a/3c$, and the critical values are at $P(0) = \frac{1}{4}b^2 \geq 0$ and $P(-2a/3c) = \frac{4}{27}\frac{a^3}{c^2} + \frac{1}{4}b^2$. Thus there are three fixed points when

$$a < -a_0 \equiv -3\left|\frac{bc}{4}\right|^{2/3}. \tag{3.10}$$

If $c = 0$, then the polynomial (3.3) is at most quadratic. It has two solutions if $a < 0$. Special cases are again shown in Table 1. Finally, when $a = b = c = 0$, there is a line of fixed points at $\xi_2 = 0$. This case (not shown in Table 1) is the only one for which there are infinitely many fixed points.

3.2. Stability. The stability properties of fixed points of the map (2.9) are most easily computed using the second difference form (2.13). Linearization about a fixed point gives the 2×2 eigenvalue problem

$$\left(\lambda C^T + \lambda^{-1} C\right) q = W q, \tag{3.11}$$

where $W = C + C^T + D^2 U(\xi)$ is the symmetric matrix

$$W = \begin{pmatrix} 2\alpha & \mu \\ \mu & 2\delta \end{pmatrix} + \begin{pmatrix} c + 6\varepsilon_2 \xi_1 & 2\xi_2 \\ 2\xi_2 & 2\xi_1 \end{pmatrix}. \tag{3.12}$$

Given the coordinate eigenvector q, the momentum components are $p = \lambda^{-1} C q$. A similar analysis can be used, more generally, for a period-n orbit; see [36, eqs. (21)–(22)].

Thus for a nontrivial solution of (3.11), the 2×2 matrix

$$N(\lambda) = \lambda C^T + \lambda^{-1} C - W$$

must be singular. Since the map is symplectic, its eigenvalues must satisfy the reflexive property: if λ is an eigenvalue, then so is λ^{-1}. This follows for (3.11) because $W^T = W$ implies that $N^T(\lambda) = N(\lambda^{-1})$. As a consequence the characteristic polynomial can be written as a quadratic polynomial in the partial trace $\rho = \lambda + \lambda^{-1}$,

$$\det(N(\lambda)) = \varepsilon_1(\rho^2 - A\rho + B - 2), \tag{3.13}$$

where we recall that $\varepsilon_1 = \det C$. The parameters A, B are Broucke's stability parameters [37, 38]. More generally, these parameters are determined by the linearized map DM at a fixed point, by $A = \operatorname{tr}(DM)$, and by $B = \frac{1}{2}\left[(\operatorname{tr}(DM))^2 - \operatorname{tr}(DM^2)\right]$; equivalently, in terms of the eigenvalues $\rho_{1,2}$ of the reduced characteristic polynomial, one has $A = \rho_1 + \rho_2$ and $B = \rho_1 \rho_2 + 2$ or, explicitly,

$$\rho_{1,2} = \tfrac{1}{2}\left(A \pm \sqrt{A^2 + 8 - 4B}\right) \equiv \lambda_{1,2} + \lambda_{1,2}^{-1}, \tag{3.14}$$

where $\lambda_{1,2}, \lambda_{1,2}^{-1}$ are the two reciprocal pairs of eigenvalues of the characteristic polynomial of the linearized map.

The (A, B)-plane is divided into seven stability regions as shown in Figure 4. These are bounded by the saddle-center (SC) and period-doubling (PD) lines,

$$\begin{aligned} SC &= B - 2A + 2 = 0, \\ PD &= B + 2A + 2 = 0, \end{aligned} \tag{3.15}$$

on which there is a pair of eigenvalues at $+1$ or -1, respectively, and the Krein parabola (KP),

$$KP = B - A^2/4 - 2 = 0, \tag{3.16}$$

on which there are double eigenvalues on the unit circle (for $B < 6$ and $|A| < 4$) or the real axis (for $B \geq 6$ and $|A| \geq 4$). The point $(A, B) = (4, 6)$ corresponds to four unit eigenvalues.

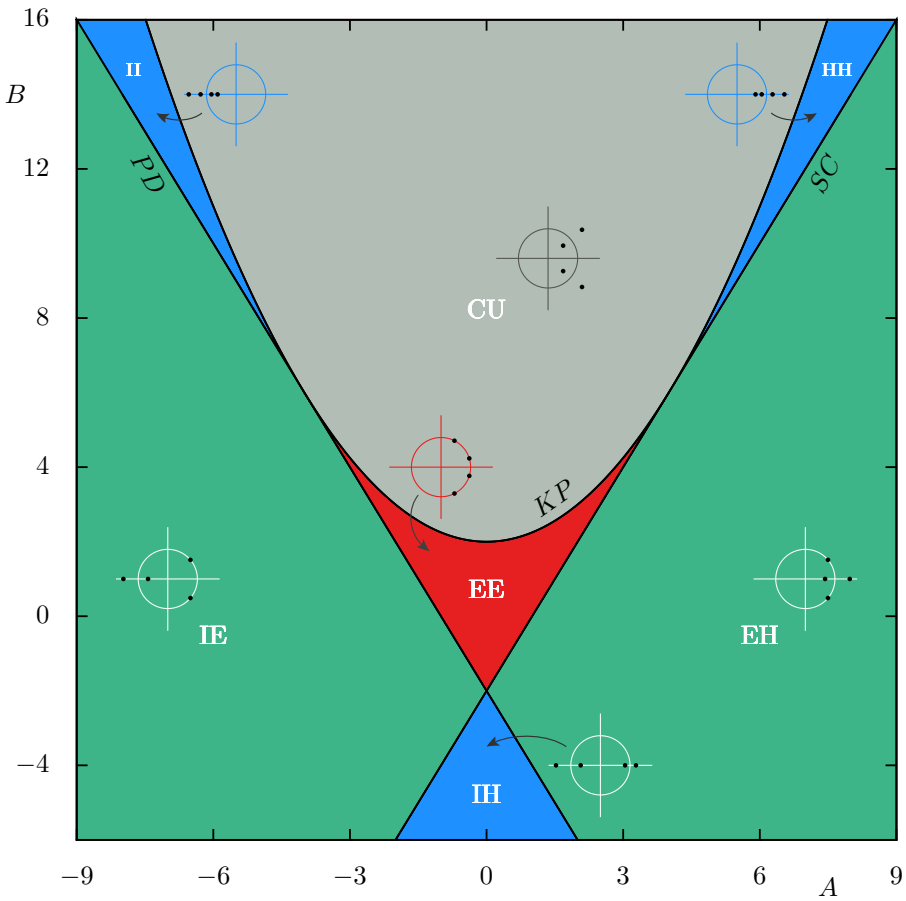

Figure 4. *Stability regions for a reflexive, quartic, characteristic polynomial. There are seven regions, EE, EH, IE, IH, II, HH, and CU, with the configuration of the four eigenvalues as shown in the representative complex plane insets.*

The seven stability regions with different types of linearized dynamics around the fixed point are labeled by combinations of E (elliptic), H (hyperbolic), and I (inverse hyperbolic), each involving a pair of eigenvalues $(\lambda, 1/\lambda)$, and in the CU (complex unstable) region, where $KP > 0$, there is a complex quartet of eigenvalues.

For a general symmetric W, the stability parameters are

$$\begin{aligned} A &= \varepsilon_1(w_{22}\alpha + w_{11}\delta - w_{12}\mu), \\ B &= \varepsilon_1(\det(W) - (\beta-\gamma)^2) + 2. \end{aligned}$$

For the matrix (3.12) these become

$$\begin{aligned} A &= 4 + \varepsilon_1\left[\delta c - (\beta-\gamma)^2 + (6\delta\varepsilon_2 + 2\alpha)\xi_1 - 2\mu\xi_2\right], \\ B &= 6 + \varepsilon_1\left[2(\delta c - (\beta-\gamma)^2) + 12\varepsilon_2(\xi_1+\delta)\xi_1 + 2(2\alpha+c)\xi_1 - 4(\xi_2+\mu)\xi_2\right], \end{aligned} \tag{3.17}$$

and the saddle-center and period-doubling parameters are

$$\begin{aligned} SC &= \varepsilon_1 \det(D^2 U) = \varepsilon_1(12\varepsilon_2\xi_1^2 + 2c\xi_1 - 4\xi_2^2), \\ PD &= 16 + 4\varepsilon_1\left(\delta c - (\beta-\gamma)^2 + 3\varepsilon_2\xi_1^2 + (6\delta\varepsilon_2 + 2\alpha + \tfrac{1}{2}c)\xi_1 - \xi_2^2 - 2\mu\xi_2\right). \end{aligned} \tag{3.18}$$

In particular, note that the sign of SC depends on the fixed points only through the sign of the Hessian of the potential (2.10); for example, if $\varepsilon_1 = 1$, then $SC > 0$ at extrema and $SC < 0$ at saddle points of U. Finally, the Krein parameter is

$$\begin{aligned} KP = &-\tfrac{1}{4}(\delta c - (\beta-\gamma)^2)^2 \\ &+ (c\delta - (\beta-\gamma)^2)(\mu\xi_2 - (3\delta\varepsilon_2 + \alpha)\xi_1) + 2\varepsilon_1 c\xi_1 \\ &+ (12\varepsilon_1\varepsilon_2 - (3\delta\varepsilon_2 + \alpha)^2)\xi_1^2 + 2\mu(3\delta\varepsilon_2 + \alpha)\xi_1\xi_2 - (\mu^2 + 4\varepsilon_1)\xi_2^2. \end{aligned} \tag{3.19}$$

At the quadfurcation, where $a = b = c = \xi_1 = \xi_2 = 0$, (3.17) gives

$$\begin{aligned} A^{\mathrm{Q}} &= 4 - \varepsilon_1(\beta-\gamma)^2, \\ B^{\mathrm{Q}} &= 6 - 2\varepsilon_1(\beta-\gamma)^2. \end{aligned} \tag{3.20}$$

This implies that the quadfurcation point lies on the saddle-center line; indeed, from (3.18), $SC = 0$ at this point. When $\varepsilon_1 = 1$ ($\varepsilon_1 = -1$), then $(A^{\mathrm{Q}}, B^{\mathrm{Q}})$ lies below and to the left of (above and to the right of) the point $(4, 6)$. The quadfurcation occurs at $(4, 6)$ only when $\beta = \gamma$, i.e., when the matrix C is symmetric; see the discussion in section 3.5 below. The quadfurcation occurs below the period-doubling line, i.e., for $PD < 0$, only if $\varepsilon_1 = 1$ and $|\beta - \gamma| > 2$.

More generally, since fixed points are critical points of U, from (3.1), they can be created or destroyed only when $\det(D^2U) = 0$, which is equivalent to $SC = 0$ by (3.18). This can also be seen upon computing the *resultant* of SC and P, (3.3)—recall that the resultant gives the set of parameters on which two polynomials simultaneously vanish. This resultant is proportional to $b^4(b^2 - b_-^2)(b^2 - b_+^2)$. Of course, this is what we saw in Figure 3—pairs of fixed points are created or destroyed upon crossing the surfaces $b = b_\pm$ (3.7).

3.3. Quadfurcation along a line in parameter space. Near the quadfurcation, if we assume that $a, b, c = \mathcal{O}(\Delta)$ for $\Delta \ll 1$, then $\xi_i = \mathcal{O}(\sqrt{\Delta})$, the cubic term involving c in (3.3) is negligible to lowest order, and the fixed points are given by (3.8) to $\mathcal{O}(\sqrt{\Delta})$. Substitution of these results into the stability criteria then gives

$$SC = \mp 4\varepsilon_1\sqrt{a^2 - 3\varepsilon_2 b^2} + \mathcal{O}(\Delta^{3/2}), \tag{3.21a}$$

$$PD = 16 - 4\varepsilon_1(\beta-\gamma)^2 + 8\varepsilon_1[(3\delta\varepsilon_2 + \alpha)\xi_1 - \mu\xi_2]\sqrt{\Delta} + \mathcal{O}(\Delta), \tag{3.21b}$$

$$KP = (\beta-\gamma)^2\left[-\tfrac{1}{4}(\beta-\gamma)^2 + (3\delta\varepsilon_2 + \alpha)\xi_1 - \mu\xi_2\right] + \mathcal{O}(\Delta). \tag{3.21c}$$

Note that the $\mp$ signs in (3.21a) correspond to the inner $\pm$ in (3.8), the sign inside the square root. Using these results, we can get an overview of all possible stability scenarios of the fixed points created in a quadfurcation; see Table 2 and Figure 5. As the quadfurcation point shifts along the SC line, different stabilities occur, but since $SC \sim \Delta$ and, generically, $PD - PD^{\mathrm{Q}} \sim \sqrt{\Delta}$, the branches emerge tangentially to the SC line (the $\mathcal{O}(\sqrt{\Delta})$ term could

Table 2

Overview of the location of the quadfurcation along the SC line depending on the value of ε_1 and the asymmetry of C. Stabilities of the fixed points are shown in the last two columns for a path of the form $(a,b,c) = \Delta(a^*,b^*,c^*)$, which has a quadfurcation at $\Delta = 0$. For $\varepsilon_2 = 1$, four fixed points are created as a becomes negative if $a < -\sqrt{3}|b|$. Their stabilities are shown in column four. When $\varepsilon_2 = -1$, two fixed points exist whenever a or $b \neq 0$ and collide at $\Delta = 0$; their stabilities are shown in the last column.

$(A^{\mathrm{Q}}, B^{\mathrm{Q}})$	Condition		Fixed points and stability	
on SC	ε_1	$\lvert\beta-\gamma\rvert$	$\varepsilon_2 = 1$, $a < -\sqrt{3}\lvert b\rvert$	$\varepsilon_2 = -1$, a or $b \neq 0$
$> (4,6)$	-1	$\neq 0$	2 EH + 2 HH	2 HH
$= (4,6)$	± 1	0	see section 3.5	see section 3.5
$< (4,6)$	1	< 2	2 EE + 2 EH	2 EH
$= (0,-2)$	1	2	IE + EE + IH + EH	IH + EH
$< (0,-2)$	1	> 2	2 IE + 2 IH	2 IH

vanish, but this is exceptional). Moreover, the sign of $A - A^{\mathrm{Q}}$ depends on the choice of the outer $\pm$ sign in (3.8), so this pair of fixed points forms a parabolic curve that is tangent to the SC line at the quadfurcation point.

Finally, note that when $\beta \neq \gamma$, $KP < 0$ at the quadfurcation, and hence a direct transition to the complex unstable (CU) region is only possible in the symmetric case for which $(A^{\mathrm{Q}}, B^{\mathrm{Q}}) = (4,6)$; this is discussed in section 3.5.

For $\varepsilon_2 = 1$ the basic structure is the one shown in the fourth column of Table 2 and in Figure 5(a),(c): four new branches emerge from a point on the saddle-center line. In each case, two of the fixed points ($SC > 0$) are above, and two ($SC < 0$) are below, this line. The implication is that when $\varepsilon_1 = 1$ and $|\beta - \gamma| > 2$, the quadfurcation occurs below the PD line and corresponds to the transition

$$\emptyset \to 2\ \mathrm{IE} + 2\ \mathrm{IH};$$

i.e., two of the created fixed points are of type IE and two are of type IH (this is not shown in Figure 5, but compare with Figure 4). Perhaps the most interesting quadfurcation creates stable fixed points. This occurs for $\varepsilon_1 = 1$ and $0 < |\beta - \gamma| < 2$, where we have the transition

$$\emptyset \to 2\ \mathrm{EE} + 2\ \mathrm{EH}. \tag{3.22}$$

This is the case shown in Figure 5(a): as Δ decreases from zero, the two created EE points move along the green and black curves in the figure, and the two EH points move along the red and blue curves.

Note that one of the EE points in this figure eventually undergoes a Krein bifurcation [39], moving into the CU region. The implication is that the Krein signature of this point must have been indefinite when it was created in the quadfurcation, since this signature is constant under parameter variations as long as the stability remains in the interior of the EE region in Figure 4 [38, sect. III].

Finally, when $\varepsilon_1 = -1$ the quadfurcation point is above $(A,B) = (4,6)$ whenever $\beta \neq \gamma$, so the transition is

$$\emptyset \to 2\ \mathrm{EH} + 2\ \mathrm{HH}. \tag{3.23}$$

This case is shown in Figure 5(c). Again, a Krein bifurcation, HH $\to$ CU, eventually occurs.

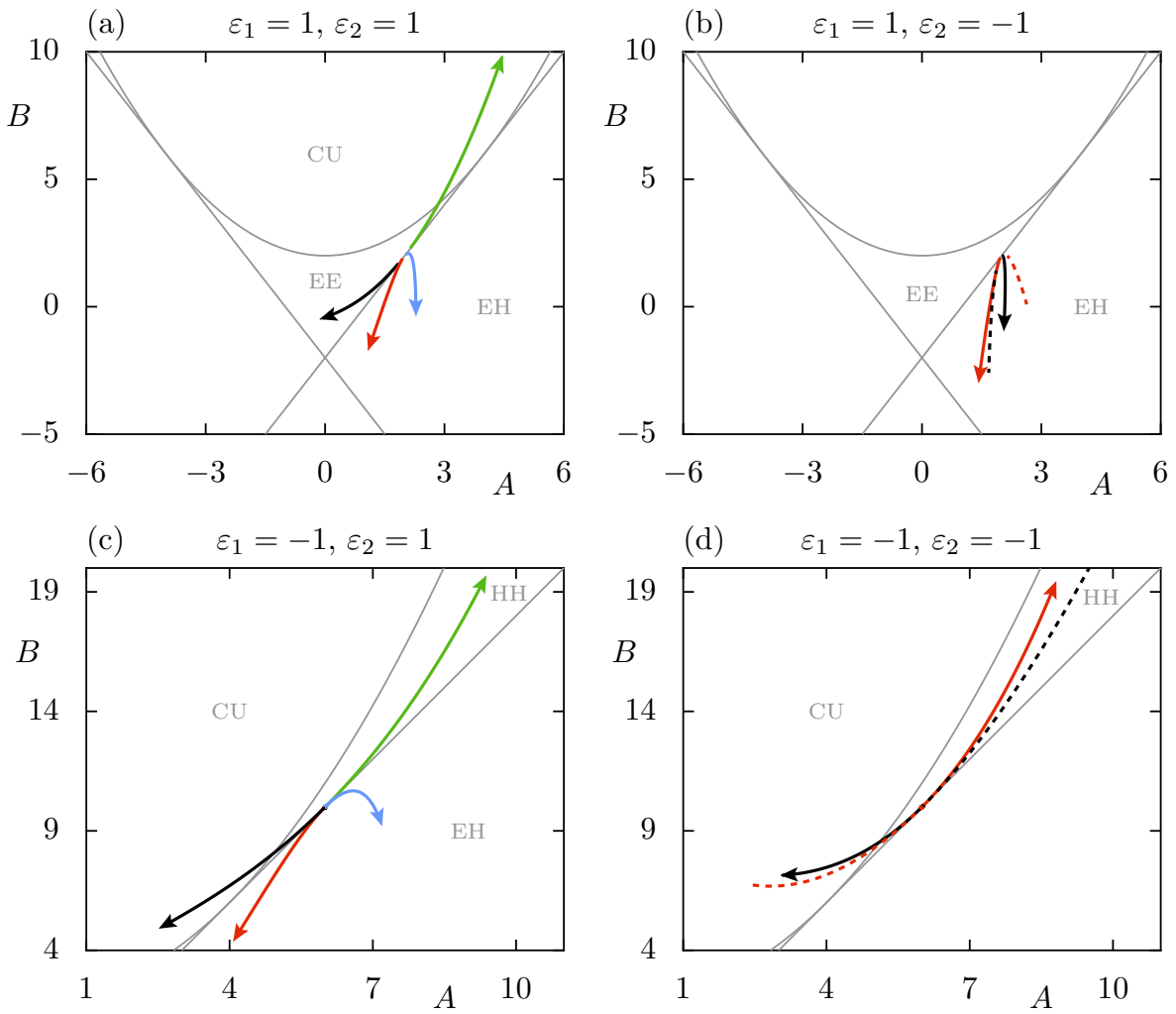

Figure 5. *Stability of fixed points for* $(a, b, c) = \Delta(1.5, 0.5, 1)$ *with* $\Delta \in [-1, 1]$ *and different choices of* C, ε_2, *and* ε_1. (a),(b) *Case* $(\alpha, \mu, \delta, \varepsilon_1) = (1, 0.1, 0.5, 1)$. *Since* $|\beta - \gamma| \approx 1.42$, *the quadrupling occurs at* $(A^Q, B^Q) = (1.99, 1.98)$. (a) $\varepsilon_2 = +1$*: creation of four fixed points in the transition* (3.22) *for* $\Delta < 0$. (b) $\varepsilon_2 = -1$*: the transition* (3.24) *before and after the bifurcation has two fixed points.* (c),(d) *Case* $(\alpha, \mu, \delta) = (1, 2.0, -0.5)$, $\varepsilon_1 = -1$, *giving* $(\beta, \gamma) \simeq (1.71, 0.29)$, *and the quadrupling occurs at* $(A^Q, B^Q) = (6, 10)$. (c) $\varepsilon_2 = 1$*: creation of four fixed points* (3.23) *for* $\Delta < 0$. (d) $\varepsilon_2 = -1$*: the transition* (3.25) *two fixed points before and after the bifurcation. The arrows indicate the direction toward more negative* Δ, *and in* (b),(d) *the branches for* $\Delta > 0$ *are shown as dashed lines.*

For $\varepsilon_2 = -1$ the basic structure is shown in the last column of Table 2 and in Figure 5(b),(d). There are two fixed points before and after the quadfurcation with positions given by the inner + sign in (3.8). Using this and (3.2), there is no sign choice that smoothly connects the (ξ_1^*, ξ_2^*) branches for $\Delta < 0$ to $\Delta > 0$: the fixed points lose their identity when they collide. The sign choice implies that $\mathrm{sgn}(SC) = -\mathrm{sgn}(\varepsilon_1)$. When $\varepsilon_1 = 1$, and hence $(A^Q, B^Q) < (4, 6)$, the fixed points both before and after the quadfurcation are below the SC

line, so the transition is

$$2\ \text{EH} \to 2\ \text{EH} \tag{3.24}$$

if $|\beta - \gamma| < 2$. As shown in Figure 5(b), the fixed points move in toward the SC line (black and red dashed curves) as $\Delta \to 0^+$, colliding at $\Delta = 0$ and splitting apart again for $\Delta < 0$ (full curves). Similarly, when $|\beta - \gamma| > 2$ the transition corresponds to

$$2\ \text{IH} \to 2\ \text{IH}.$$

Finally, when $\varepsilon_1 = -1$ and $(A^{\text{Q}}, B^{\text{Q}}) > (4, 6)$, the transition is

$$2\ \text{HH} \to 2\ \text{HH}, \tag{3.25}$$

as shown in Figure 5(d).

It is interesting that all of this structure is quite different from what would be expected from a pair of decoupled, area-preserving maps undergoing saddle-center bifurcations, where there can be at most one EE point. This case corresponds to the special point $(A^{\text{Q}}, B^{\text{Q}}) = (4, 6)$, which will be treated in section 3.5 and applied to the case of decoupled maps in section 6.

3.4. Two to four fixed point transitions. When a parameter path crosses one of the surfaces $b_\pm(a, c)$, then $SC = 0$ in (3.18), and the resulting saddle-center bifurcation typically creates or annihilates a pair of new fixed points, one with E eigenvalues and one with H eigenvalues. When $\varepsilon_2 = -1$, there are two fixed points outside the wedge between b_+ and b_- shown in Figure 3(b), and so if the parameter path enters the wedge, then two new fixed points are created. If the path enters the wedge at the quadfurcation point $a = b = c = 0$, then the two existing fixed points merge, and the bifurcation—now a quadfurcation—occurs at the origin. Depending upon $\beta - \gamma$ and the sign ε_1, the quadfurcation can occur at any point along the SC line, and so a number of different stability cases can arise.

An example is shown in Figure 6 for the parabolic path

$$(a, b, c) = (-0.07 \cdot \Delta|\Delta|, 0.01 \cdot \Delta^2, \Delta) \tag{3.26}$$

as Δ varies, with the remaining parameters as described in the caption. Figure 6 shows the contours of the potential for $\Delta = -0.5, 0$, and 1, and Figure 7 shows the corresponding stability diagram. There are two fixed points when $\Delta < 0$, both of type EH; these merge at $\Delta = 0$. The quadfurcation corresponds to a transition,

$$2\ \text{EH} \to 3\ \text{EH}\ + \text{EE}.$$

Effectively the original EH pair is reformed, and the contour lines near the new EE–EH pair in Figure 6(c) resemble those for a local saddle-center bifurcation.

3.5. Krein collisions, symmetric C, and reversibility. As we noted in (3.20), the quadfurcation occurs for a multiplicity-four unit eigenvalue only when the matrix C of (2.3) is symmetric. This is the only case in which the quadfurcation can immediately create fixed points of type CU; recall Figure 4.

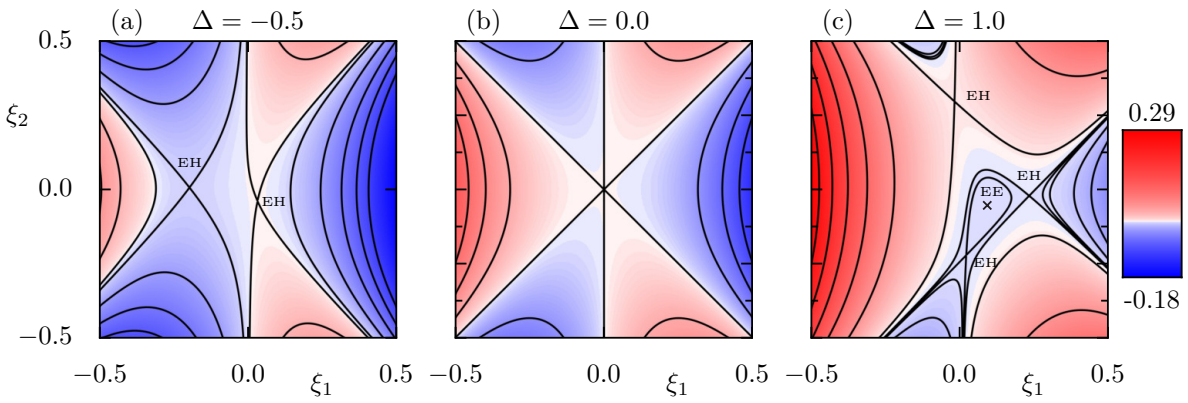

Figure 6. *Contour plots of the potential U from (2.10) for the path (3.26) with $(\alpha, \mu, \delta) = (1, 0.1, 0.5)$, $\varepsilon_1 = 1$, and $\varepsilon_2 = -1$. The three panels show $\Delta = -0.5, 0$, and 1. Two EH fixed points merge in the quadfurcation at $\Delta = 0$, and for $\Delta > 0$ there are four fixed points, where one is EE and three are EH.*

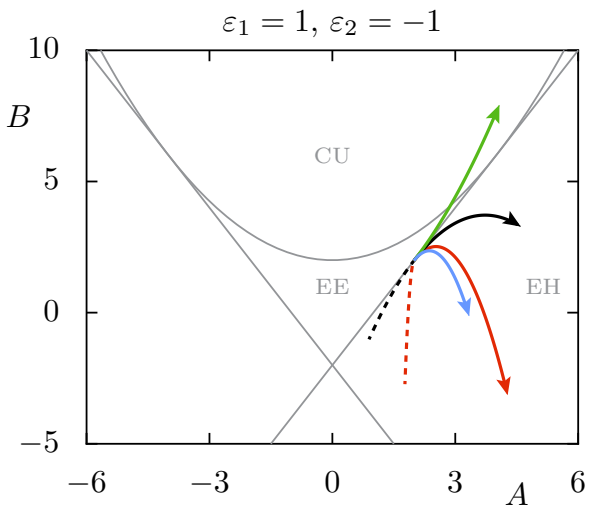

Figure 7. *Stability diagram for the path (3.26) with $\Delta \in [-2, 5]$ and for all other parameters as in Figure 6. The two EH fixed points for negative Δ (dashed curves) merge at the quadfurcation point $\Delta = 0$ and lead to four fixed points for $\Delta > 0$, one with EE and three with EH stability. For larger Δ the EE point becomes type CU.*

As discussed in section 2.3 the inverse of the Moser map is conjugate to the original map upon the replacement $C \to C^T$. Therefore, when C is symmetric, the map (2.2) is reversible, i.e., it is conjugate to its inverse [40]; thus, $S \circ f = f^{-1} \circ S$ for a homeomorphism S. For example, the Hénon map (2.1) is reversible with $S(x, y) = (y, x)$. In general, the inverse of (2.9) is

$$M^{-1}(\xi, \eta) = \left(C^{-1}\eta, \eta + C^T(-\xi + C^{-1}\eta) + \nabla U(C^{-1}\eta)\right).$$

This map is conjugate to M when $C = C^T$ using the reversor

$$S(\xi, \eta) = (C^{-1}\eta, C\xi).$$

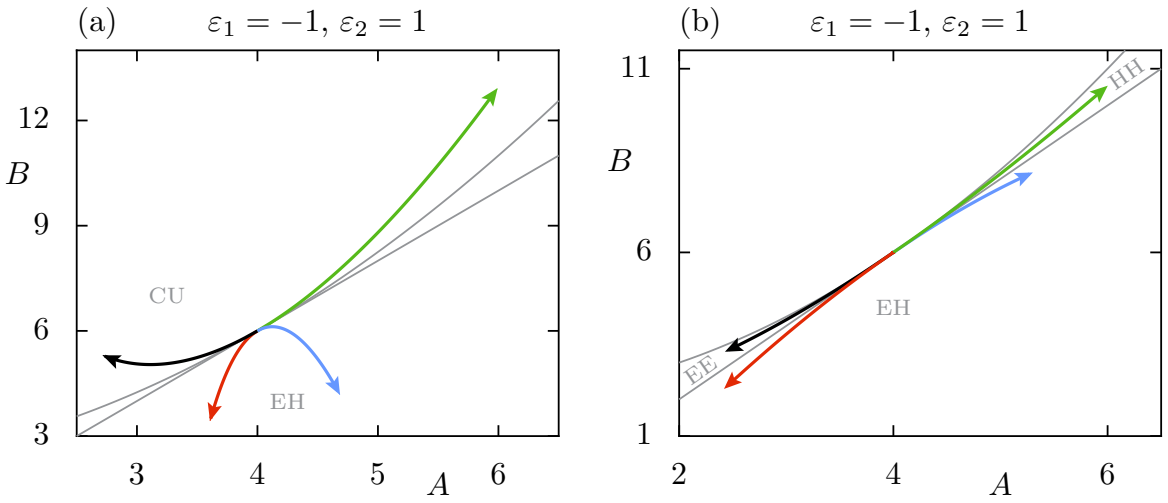

Figure 8. *Stability of fixed points for symmetric C with $\varepsilon_1 = -1$ and $\varepsilon_2 = +1$. The parameters vary along the line $(a, b, c) = \Delta(\frac{3}{2}, \frac{1}{2}, 1)$ with $\Delta \in [-1, 0]$.* (a) *The transition* (3.27) *for* $(\alpha, \mu, \delta) = (-\frac{3}{2}, 1, \frac{1}{2})$, *giving* $\beta = \gamma = \frac{1}{2}$. (b) *The transition* (3.28) *for* $(\alpha, \mu, \delta) = (\frac{3}{2}, \sqrt{\frac{23}{2}}, \frac{5}{4})$, *giving* $\beta = \gamma = \sqrt{\frac{23}{8}}$.

Thus, as Moser showed [31], if C is symmetric, the map (2.2) or, equivalently, (2.9), is reversible; we do not know if the converse of this statement is true. This reversor is an involution with the fixed set $\mathrm{Fix}(S) = \{(\xi, C\xi) : \xi \in \mathbb{R}^2\}$, a 2D plane. All of the fixed points are thus symmetric.

The quadfurcation is especially interesting in the reversible case since, by (3.17) and (3.21), only then does it occur for the stability parameters $(A^{\mathrm{Q}}, B^{\mathrm{Q}}) = (4, 6)$. Indeed, as in section 3.3, assuming that $a, b, c = \mathcal{O}(\Delta)$ and $\xi_i = \mathcal{O}(\sqrt{\Delta})$ near the quadfurcation, the Krein criterion (3.21c) is zero to $\mathcal{O}(\Delta^{1/2})$, and the first nonzero terms are

$$KP = 4\alpha\delta a - 2(\alpha + 3\varepsilon_2\delta)\gamma b + \left(12\varepsilon_1\varepsilon_2 - (\alpha - 3\varepsilon_2\delta)^2\right)\xi_1^{*2} + \mathcal{O}\left(\Delta^{3/2}, (\beta - \gamma)^2\right),$$

where ξ_1^* is given by (3.8). The sign of this parameter can change, depending upon the details. However, note that since KP depends only on ξ_1^{*2}, it does not depend upon the outer sign in (3.8). Thus when $c = \mathcal{O}(\Delta)$, the fixed points come in pairs with the same sign of KP.

When $\varepsilon_2 = 1$, the four created fixed points come in pairs with opposite signs of SC from (3.21a). Thus there will be a pair of fixed points of type EH. Since the curves generically emerge tangent to the SC line, either both points in the second pair will have type CU, or one will be EE and the other HH. For example, a quadfurcation of the form

$$\emptyset \to 2\ \mathrm{CU} + 2\ \mathrm{EH} \tag{3.27}$$

is shown in Figure 8(a). For this case, $KP = \frac{1}{4}(3 \pm 7\sqrt{6})\Delta$ to lowest order, where the sign is the inner $\pm$ sign in (3.8), implying that the two fixed points with the $+$ sign have $KP > 0$ when $\Delta < 0$ near the quadfurcation and are thus of type CU. In contrast, for the example shown in Figure 8(b) the quadfurcation is

$$\emptyset \to\ \mathrm{EE} + \mathrm{HH} + 2\ \mathrm{EH}, \tag{3.28}$$

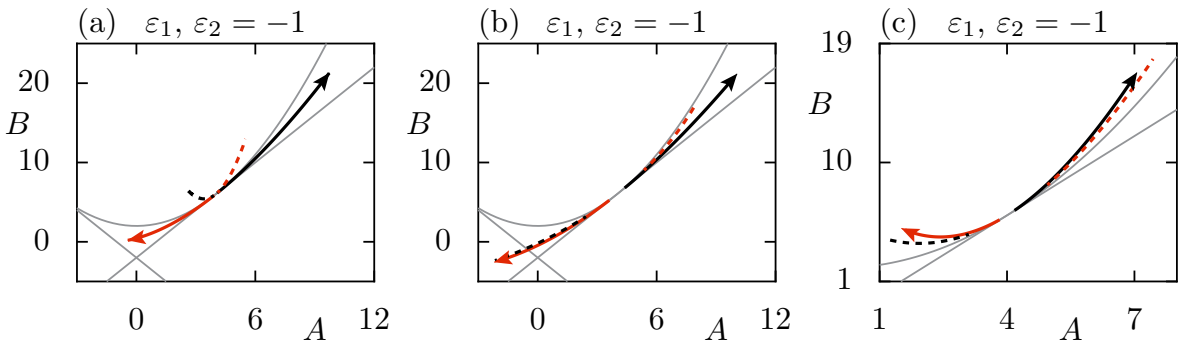

Figure 9. *Stability of fixed points for symmetric C and $\varepsilon_1 = \varepsilon_2 = -1$. The parameters $(a, b, c) = \Delta(\frac{3}{2}, \frac{1}{2}, 1)$ for* (a) *and* (b)*, and $\Delta(2, \frac{1}{2}, 1)$ for* (c)*, with $\Delta \in [-\frac{1}{2}, \frac{1}{2}]$. The arrows indicate the direction towards more negative Δ, and branches for $\Delta > 0$ are shown as dashed lines.* (a) *The transition* (3.29) *for $(\alpha, \mu, \delta) = (\frac{1}{2}, \sqrt{6}, 1)$, giving $\beta = \gamma = \sqrt{\frac{3}{2}}$.* (b) *The transition* (3.30) *for $(\alpha, \mu, \delta) = (\frac{99}{16}, -\frac{5}{2}, \frac{1}{11})$, giving $\beta = \gamma = -\frac{5}{4}$.* (c) *The transition* (3.31) *for $(\alpha, \mu, \delta) = (-\frac{3}{2}, 1, \frac{1}{2})$, giving $\beta = \gamma = \frac{1}{2}$.*

as here $KP = \frac{\Delta}{64}(993 - 84\sqrt{46} \pm 91\sqrt{6}) < 0$ when the fixed points exist, i.e., when $\Delta < 0$. This last case shows what would happen in a pair of uncoupled 2D maps, and it can be seen in section 6.

As in section 3.3, when $\varepsilon_2 = -1$, the quadfurcation at $\Delta = 0$ corresponds to a collision and re-emergence of a pair of fixed points with $\operatorname{sgn}(SC) = -\operatorname{sgn}(\varepsilon_1)$. When $\varepsilon_1 = 1$, all of the fixed points will have stability type EH, and so the transition is

$$2\ \mathrm{EH} \to 2\ \mathrm{EH}$$

and thus follows the pattern shown in Figure 5(b).

However, when $\varepsilon_1 = -1$, $\operatorname{sgn}(SC) = +1$, implying that EE, HH, and CU are all possible. However, since the two fixed points have the + inner sign in (3.8), they will have the same sign of KP, so we have either a CU pair or an EE+HH pair. The possible transitions are

$$2\ \mathrm{CU} \to\ \mathrm{EE} + \mathrm{HH}, \tag{3.29}$$

for which the stability diagram is shown in Figure 9(a),

$$\mathrm{EE} + \mathrm{HH} \to\ \mathrm{EE} + \mathrm{HH}, \tag{3.30}$$

with the stability diagram shown in Figure 9(b), and

$$2\ \mathrm{CU} \to 2\ \mathrm{CU}, \tag{3.31}$$

with the stability diagram shown in Figure 9(c).

Another technique for analyzing stability in the neighborhood of the quadfurcation is to use the ODE limit (2.16) with the Hamiltonian (2.18). Recall that this limit assumes that we use the scaling $(a, b, c) \to (h^4 a, h^4 b, h^2 c)$ for $h \ll 1$. This scaling differs from the Δ-scaling by allowing larger relative values for c. The implication of this is that the term $\frac{1}{2}cq_1^2$ in U, which

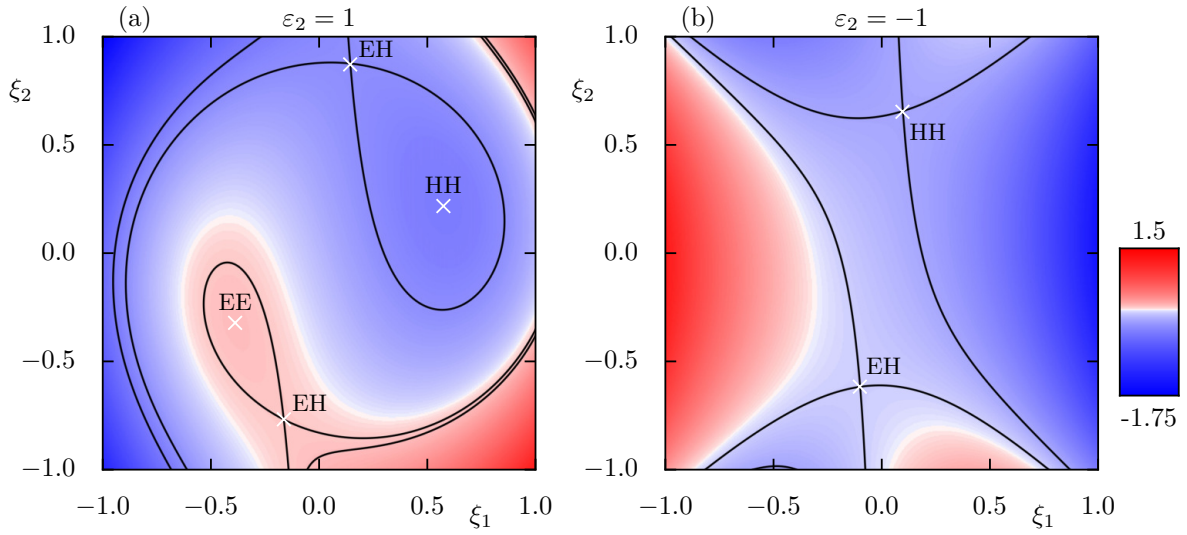

Figure 10. *Contour plot of the potential U from (2.10). (a) For $(a,b,c) = (-\frac{3}{4}, -\frac{1}{4}, -\frac{1}{2})$ and $\varepsilon_2 = 1$ there are four critical points, which are equilibria of (3.32). When $C > 0$, the maximum, at $\xi = (-0.38825, -0.32196)$, corresponds to a doubly elliptic equilibrium, and the minimum, at $\xi = (0.57441, 0.21761)$, to a doubly hyperbolic equilibrium. As a specific example, $(\alpha, \mu, \delta) = (\frac{5}{2}, \sqrt{6}, 1)$, is used for the matrix C determining the stabilities.* (b) *Potential for $(a,b,c) = (-\frac{3}{8}, -\frac{1}{8}, -\frac{1}{4})$ and $\varepsilon_2 = -1$, where there are two critical points; the matrix C, determining the stabilities, is the same as in* (a).

was negligible when $c = \mathcal{O}(\Delta)$, is formally important when we take $c = \mathcal{O}(h^2)$. When C is symmetric, $C^{\mathrm{a}} = 0$, and the Coriolis and centripetal-like terms vanish, simply giving

$$H(q,p) = \tfrac{1}{2} p^T C^{-1} p - U(q). \tag{3.32}$$

When $C = C^{\mathrm{s}}$ is positive or negative definite, the stability is governed entirely by the classification of the critical point of U. In particular if $C > 0$, then since the potential in (2.18) is $-U$, a minimum of U is an HH point, and a maximum is an EE point. Saddles correspond to EH points. When $C < 0$, the minima are HH and the maxima are EE. This is more generally consistent with (3.18), which shows that $SC = \varepsilon_1 \det(D^2 U)$. Two example contour plots for U are shown in Figure 10.

4. Elliptic bubbles. To visualize the dynamics near the fixed points of the 4D map, we use a 3D *phase space slice* [41]. In its simplest form, this is a thickened 3D hyperplane in the 4D phase space defined by fixing one of the coordinates, e.g., $\eta_2 = \eta_2^\star$, to define the slice of thickness ϵ by

$$\left\{ (\xi_1, \xi_2, \eta_1, \eta_2) \;\middle|\; |\eta_2 - \eta_2^*| \le \epsilon \right\}.$$

Whenever the points of an orbit lie within the slice, the remaining coordinates (ξ_1, ξ_2, η_1) are displayed in a 3D plot. The parameter ϵ determines the resolution of the resulting plot; decreasing ϵ requires the computation of longer trajectories as the slice condition is fulfilled less often, but the resulting intersections will be more precise. For example, if a two-torus intersects the hyperplane, it will typically do so in one or more loops. As ϵ grows, these

loops thicken into annuli in the slice. For further examples and detailed discussions, see [41, 42, 43, 44, 45, 46].

For our purposes a slightly more general, rotated slice, defined so as to contain all of the fixed points, will be more convenient. Because the momenta of the fixed points are determined by the coordinates through $\eta = C\xi$, all fixed points of the 4D map (2.9) are contained in a 2D plane. Following the ideas of [41, App. 3], we define new coordinates (ξ, χ), with $\chi = \eta - C\xi$, so that the fixed points lie in the two-plane $\chi = 0$. Thus we define the 3D slice

$$\Gamma_\epsilon = \{(\xi_1, \xi_2, \chi_1, \chi_2) \mid |\chi_2| \le \epsilon\}$$

so that we get (ξ_1, ξ_2, χ_1) as 3D coordinates. Equivalently, this corresponds to using nonorthogonal basis vectors given as columns of the block matrix

$$B = (\mathrm{v}_1|\mathrm{v}_2|\mathrm{v}_3|\mathrm{v}_4) = \begin{pmatrix} I & 0 \\ C & I \end{pmatrix}.$$

As these are linearly independent, they can be used to express any point as a linear combination with coefficients $(\xi_1, \xi_2, \chi_1, \chi_2)$. These coefficients can be computed from the scalar products with the dual basis vectors $\{\mathrm{v}^i\}$, which are the columns of

$$B^{-T} = (\mathrm{v}^1|\mathrm{v}^2|\mathrm{v}^3|\mathrm{v}^4) = \begin{pmatrix} I & -C^T \\ 0 & I \end{pmatrix}.$$

Figure 11 shows an example of a slice for the map (2.9) with the parameters of Figure 5(a) when $\Delta = -0.01$. For these parameters the quadfurcation has created two EE and two EH fixed points that, by construction of the 3D slice, lie in the 2D plane $\chi_1 = 0$. As expected from KAM theory, the EE fixed points should be surrounded by a Cantor family of two-tori on which the dynamics is conjugate to incommensurate rotation. By analogy with Moser's theorem for 2D maps [47], the density of these tori should approach 1 as they limit on the EE points, provided that the linearized frequencies are not in a low-order resonance. Indeed, the formal normal form expansion around a nonresonant EE point is an integrable twist map to all orders [21], and higher-dimensional results along the lines of Moser's twist theorem have been proven for elliptic equilibria of Hamiltonian flows [48, 49]. In the 3D slice each of these tori becomes two (or more) thin annular rings, which, since we have set $\epsilon = 10^{-6}$, appear as 1D loops in the figure [41].

The numerical approximations of regular tori in Figure 11 were obtained by manually choosing initial conditions in several 2D planes in the 3D slice so that the tori appeared to represent a kind of "outer" boundary of the regular region. Some initial conditions escape quickly and are discarded. We numerically verified that these sets are 2D tori using frequency analysis [50, 51, 41]. Here one computes, for a finite trajectory segment, two fundamental frequencies from a windowed Fourier transform; on a true torus, these should be independent of the segment chosen. All but two of the tori in Figure 11 have frequencies that vary by less than 7×10^{-7} when computed over successive segments of 4096 iterates, and for most the variation is of order 10^{-10}. The two exceptional "tori" in the figure have a frequency variation of order 2×10^{-5} and are probably very weakly chaotic orbits that are trapped near a resonance for long times by Nekhoroshev stability.

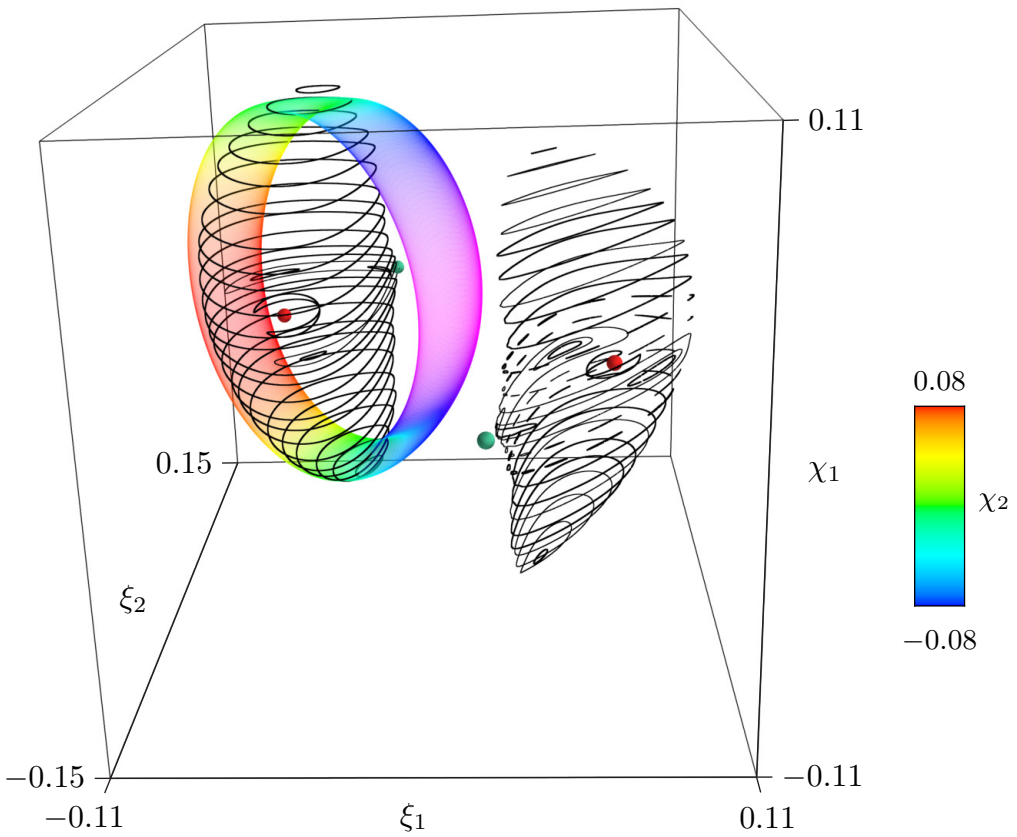

Figure 11. *Three-dimensional phase space slice of the* 4D *map corresponding to Figure* 5(a) *with parameters* $(\alpha, \mu, \delta) = (1, 0.1, 0.5)$, $\varepsilon_1 = \varepsilon_2 = 1$, *and* $(a, b, c) = (-0.015, -0.005, -0.01)$. *The small spheres show two EE (red) and two EH (green) fixed points. Also shown are several selected regular tori (black lines) surrounding the EE fixed points. Each torus is represented by* 10^4 *points in the slice with* $\epsilon = 10^{-6}$. *These tori are* 2D *in the* 4D *phase space and therefore (usually) lead to a pair of loops in the* 3D *phase space slice. A projection of one* 2D *torus is shown as* 10^6 *semitransparent points with* χ_2 *encoded in color (see color bar). For a rotating view, see* M126866_01.mp4 [local/web 21.6MB].

This family of two-tori appears to be approximately limited by the locations of the EH fixed points. Indeed, since the center-stable and center-unstable manifolds of the EH points are 3D, they should form boundaries for the elliptic dynamics. Of course, we expect that there will be chaotic orbits near these manifolds, and so the regular 2D tori will not extend into the chaotic zone. Figure 11 also shows the full orbit of one of these 2D tori, now *projected* onto the slice; the projected coordinate χ_2 is encoded in color as indicated in the color bar on the right [52].

Figure 12 shows an example of a slice for the transition (3.30) for the case when the matrix C is symmetric; the parameters correspond to Figure 9(b) with $\Delta = -0.001$, close to the quadfurcation. For this case there are only two fixed points, one of type EE and the other

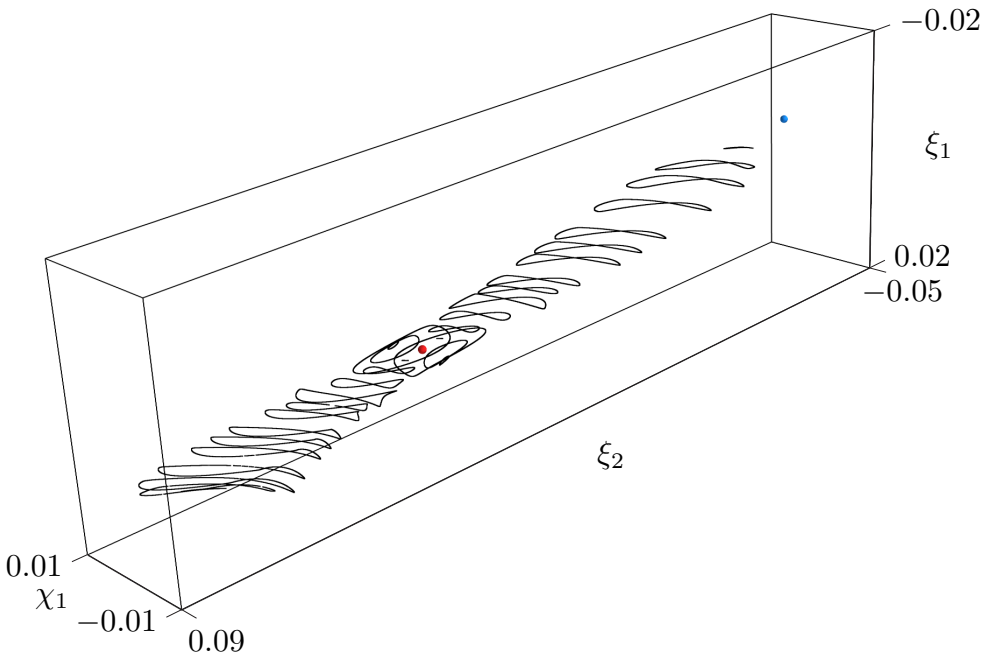

Figure 12. 3D *phase space slice of the* 4D *map for parameters of Figure* 9(b) *with* $\Delta = -0.001$. *The small spheres show an EE (red) and an HH (blue) fixed point. Also shown are slices of several selected regular tori as in Figure* 11. *For a rotating view see* M126866_02.mp4 [local/web 6.33MB].

of type HH. Here again we see a family of 2D tori surrounding the EE point. This family has a larger extent in the ξ_2 direction than in ξ_1, and the loops shrink in size as they become closer to the HH point. Note that now the stable and unstable manifolds of the HH point are two-dimensional and so do not form barriers in 4D.

5. Bounded orbits. Moser showed, under a nondegeneracy condition on the quadratic terms, that the domain of the quadratic map containing bounded orbits is itself bounded [31]. To obtain an explicit bound we consider the second-difference form (2.13), rewriting it as

$$C^T \xi_{t+1} + C\xi_{t-1} = A + D\xi_t + Q(\xi_t), \tag{5.1}$$

where $A = (a, b)^T$ is a constant vector and the linear and quadratic terms are

$$D\xi \equiv \begin{pmatrix} 2\alpha + c & \mu \\ \mu & 2\delta \end{pmatrix} \begin{pmatrix} \xi_1 \\ \xi_2 \end{pmatrix},$$
$$Q(\xi) \equiv \begin{pmatrix} 3\varepsilon_2 \xi_1^2 + \xi_2^2 \\ 2\xi_1 \xi_2 \end{pmatrix}.$$

Using this form we can prove the following.

Theorem 1. *When* $\varepsilon_2 = \pm 1$, *all orbits that are bounded for both positive and negative times*

of the map (5.1) *are contained in the disk* $\|\xi\| \le \kappa$, *where*

$$\kappa \equiv \tfrac{1}{2\tau}\left(\kappa_2 + 2\kappa_3 + \sqrt{(\kappa_2+2\kappa_3)^2 + 4\tau\sqrt{a^2+b^2}}\right), \tag{5.2}$$

with $\tau = 1$ *for* $\varepsilon_2 = 1$ *and* $\tau = \sqrt{\frac{2}{3}}$ *for* $\varepsilon_2 = -1$, *and we define*

$$\begin{aligned} \kappa_2 &\equiv \|D\|_F = \sqrt{(2\alpha+c)^2 + 2\mu^2 + 4\delta^2}, \\ \kappa_3 &\equiv \|C\|_F = \sqrt{\alpha^2+\beta^2+\gamma^2+\delta^2}. \end{aligned} \tag{5.3}$$

Proof. When $\varepsilon_2 = 1$, the norm of the quadratic terms has the lower bound

$$\|Q(\xi)\|^2 = 9\xi_1^4 + 10\xi_1^2\xi_2^2 + \xi_2^4 = (9\xi_1^2+\xi_2^2)\|\xi\|^2 \ge \|\xi\|^4 = \rho^4,$$

where we denote $\|\xi\| = \rho$.

Using the triangle inequality on (5.1) gives

$$\|C^T\xi_{t+1}\| + \|C\xi_{t-1}\| \ge \|Q(\xi_t)\| - \|D\xi_t\| - \|A\|. \tag{5.4}$$

Define $\kappa_{2,3} > 0$ so that

$$\|D\xi_t\| \le \kappa_2\rho_t; \quad \|C^T\xi_t\|, \|C\xi_t\| \le \kappa_3\rho_t.$$

For example, we can use the Frobenius norms of these matrices to give (5.3) (one could also use the operator norm, giving results in terms of the singular values). Putting the bounds into (5.4) gives

$$\kappa_3(\rho_{t+1} + \rho_{t-1}) \ge \rho_t^2 - \kappa_2\rho_t - \|A\|. \tag{5.5}$$

Let $\kappa > 0$ be chosen such that whenever $\rho > \kappa$, we have $\rho^2 - \kappa_2\rho - \|A\| > 2\kappa_3\rho$. Solving for the largest root of this quadratic, as an equality, gives (5.2). Using this in (5.5) implies that whenever $\rho_t > \kappa$,

$$\rho_{t+1} + \rho_{t-1} > 2\rho_t. \tag{5.6}$$

Thus, if $\rho_t > \kappa$, there are two possible cases as follows:

- Suppose that $\rho_t \ge \rho_{t-1}$. Then by (5.6), we have $\rho_{t+1} > 2\rho_t - \rho_{t-1} \ge \rho_t$. This implies that the sequence $\{\rho_t\}$ is strictly increasing with t. If this monotone sequence is bounded, it must approach a limit $\rho_t \to \rho^*$, which must be a solution of (5.5) as an equality. But this implies that ρ^* is no more than the largest root κ, contradicting our assumption. Thus $\{\rho_t\}$ is unbounded as $t \to \infty$.
- Alternatively, suppose that $\rho_t < \rho_{t-1}$. Relabeling the t index in (5.6) then implies that $\rho_{t-2} > 2\rho_{t-1} - \rho_t > \rho_{t-1}$. Thus the sequence $\{\rho_t\}$ strictly increases as t decreases. Again, since $\rho_t > \kappa$, this implies that ρ_t is unbounded, now as $t \to -\infty$.

Together, these imply the theorem for the case that $\varepsilon_2 = 1$.

If $\varepsilon_2 = -1$, then we can see that $\|Q(\xi)\|^2 \geq \frac{2}{3}\rho^4$; indeed,

$$\|Q(\xi)\|^2 - \frac{2}{3}(\xi_1^2 + \xi_2^2)^2 = \frac{25}{3}\xi_1^4 - \frac{10}{3}\xi_1^2\xi_2^2 + \frac{1}{3}\xi_2^4 = \frac{1}{3}(5\xi_1^2 - \xi_2^2)^2 \geq 0.$$

Thus the analysis above works if we replace κ by the larger solution to

$$\tau\rho^2 - (\kappa_2 + 2\kappa_3)\rho - \|A\| = 0,$$

with $\tau = \sqrt{\frac{2}{3}}$, giving (5.2) again. ∎

Note that if $\varepsilon_2 = 0$, then

$$\|Q(\xi)\|^2 = 4\xi_1^2\xi_2^2 + \xi_2^4 = \xi_2^2(4\xi_1^2 + \xi_2^2),$$

which does not obey a bound of the form needed in the proof of Theorem 1. Thus the theorem does not apply to this case. Indeed, we showed in section 3.1 that if $\varepsilon_2 = 0$, then when $a = b = c = 0$ there is a line of fixed points; recall the discussion in section 3.1.

A good way to visualize the distinction between bounded and unbounded orbits for a given parameter set is via an escape time plot; see Figure 13. In this plot, a grid of initial points of the form $(\xi, \eta) = (\xi, C\xi)$ is iterated until $\|\xi\| > \kappa$, and the required time to escape is encoded in color. Points that have not escaped within 10^4 iterations are displayed in white. Some of these points lie on a family of regular 2D tori in the neighborhood of the EE fixed point; these will never escape. Points near the boundary of the white region may eventually escape, and, indeed, even arbitrarily close to an EE fixed point there are initial conditions that are expected to escape for extremely large times by means of Arnold's exponentially slow diffusion mechanism [53, 54, 55, 56].

We can quantify the size of the region of "bounded orbits" under parameter variation by computing the area of the white region in a 2D-plane of initial conditions like that in Figure 13. For this we choose initial conditions in the two-plane $(\xi, C\xi)$, with ξ varied on a grid of 3000×3000 points within the box $-\frac{1}{2}\kappa < \xi_i < \frac{1}{2}\kappa$, and iterate at most 5000 steps. Orbits that remain within the disk $\|\xi\| \leq \kappa$ are counted, and the resulting area is denoted A_{reg}. This area varies as fixed points undergo various bifurcations. A 1D cut through parameter space (see Figure 14) shows how A_{reg} varies with the parameter a (here $b = c = 0.01$). Insets in the figure show escape time plots, like that in Figure 13, for some selected parameters. There is a strong correlation of the area with the structure of the region of stable orbits around the EE point, as we discuss further below.

In Figure 15 we show A_{reg} as a function of the two parameters a and b, setting $c = b$. Note that there are apparently no bounded orbits when $b > b_+$ (3.7), where there are no fixed points, nor when $b \gtrsim 0.6$ or $a < -1.5$. The largest bounded area occurs in the region near the origin in the (a, b) plane; recall that the origin corresponds to the quadfurcation since $c = b$. The dotted curve corresponds to parameters for which $PD = 0$, the period-doubling bifurcation (3.21b). To the left of the PD curve, the EE fixed point becomes IE and A_{reg} decreases quickly to 0. To the right of the PD curve and for $b < b_-$, the four fixed points have the stabilities EE, EH, EH, and CU. On the curve $b = b_-$, the EH and CU fixed points

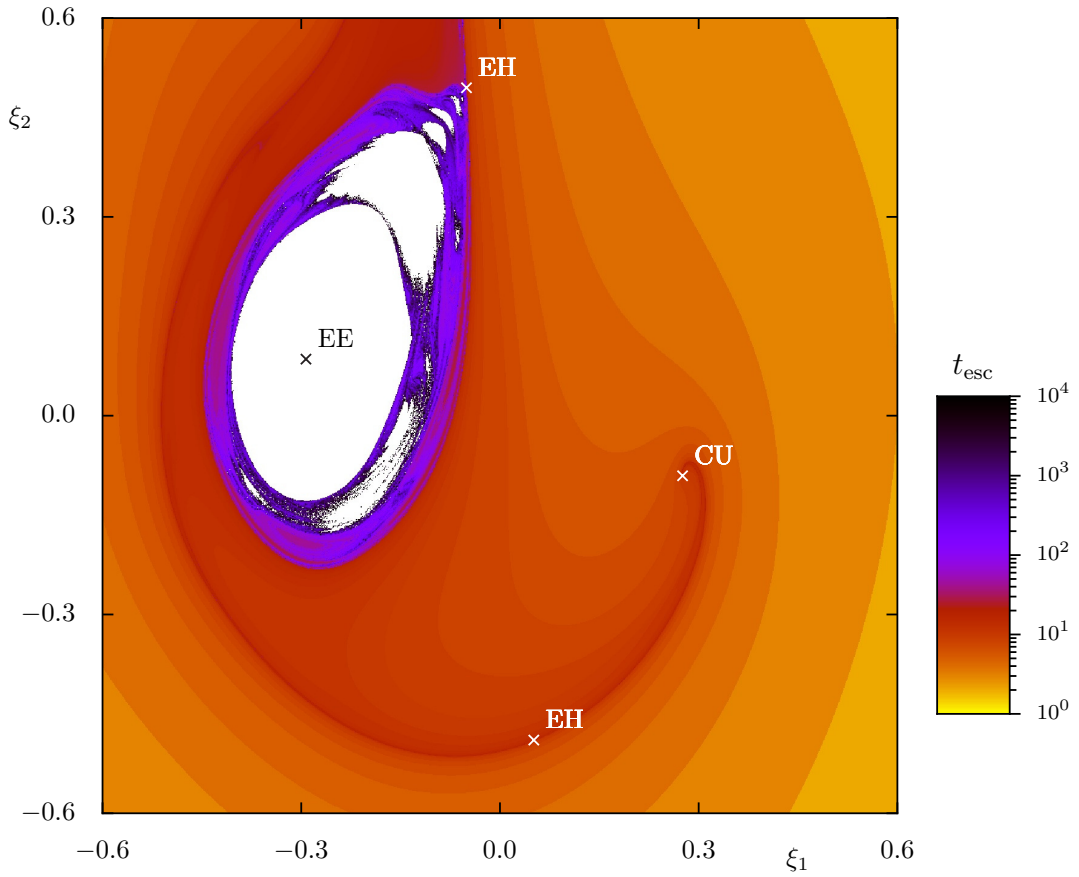

Figure 13. *Plot of the escape time t_{esc} encoded in color for initial conditions defined via (ξ_1, ξ_2) with $\eta = C\xi$. Initial conditions whose orbits have not escaped within 10^4 iterations are colored white. There is a large region of nonescaping orbits surrounding the EE fixed point. Further from the EE point, one observes a complicated fine-scale structure of escaping and nonescaping orbits. Parameters are $(\alpha, \mu, \delta) = (1, 0.1, 0.5)$, $\varepsilon_1 = \varepsilon_2 = 1$, and $(a, b, c) = (-0.25, 0.05, 0.05)$.*

coalesce; however, since there are no bounded, regular orbits in a neighborhood of these fixed points, this transition does not influence $A_{\rm reg}$.

At several places in Figure 14 and along several curves in Figure 15, one observes a substantial decrease in the bounded area. Several of these decreases can be related to those parameters for which the linearization about the elliptic-elliptic fixed point fulfills a low-order resonance. Of course, such behavior is well known for the case of 2D area-preserving maps. The variation is related to the fractal structure of the stability region, which changes significantly, in particular when passing through the low-order resonances; see, e.g., [57, 58, 59].

At a resonance in the 4D case, the four eigenvalues have the form $\lambda_{1,2} = \mathrm{e}^{2\pi \mathrm{i} \nu_{1,2}}$, and the conjugate/inverse values the form $\bar{\lambda}_i = 1/\lambda_i$. Each frequency, ν_i, describes the rate of rotation around the fixed point in the 2D invariant planes spanned by the eigenvectors of the corresponding conjugate pair of eigenvalues. These can be written in terms of the partial

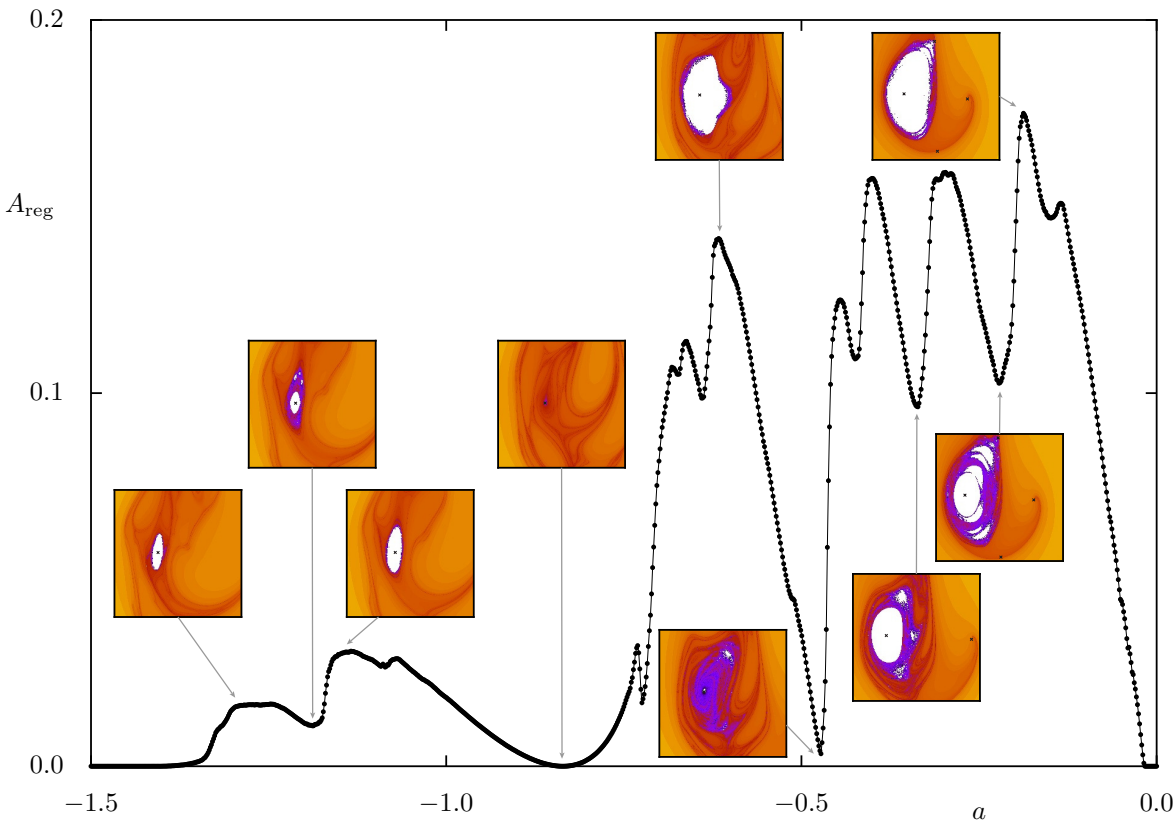

Figure 14. *Area of bounded initial conditions $(\xi, C\xi)$, determined from a grid in the ξ-plane for $|\xi_i| < \kappa/2$, under variation of a with $b = c = 0.01$, and $\varepsilon_2 = 1$; the matrix C is as in Figure 13. The insets show escape time plots for a neighborhood of the EE fixed point. Note that for all a-values in the figure there are four fixed points (shown as small black crosses in the insets), which, as a decreases, move out of the shown square. A movie of escape time plots as a function of a can be found in* M126866_03.mp4 [local/web 9.80MB].

traces, $\rho_{1,2}$ (recall (3.14)), as

$$\nu_{1,2} = \frac{1}{2\pi} \arccos\left(\frac{1}{2}\rho_{1,2}\right).$$

The frequencies (ν_1, ν_2) of an EE fixed point fulfill a resonance condition when

$$n_1\nu_1 + n_2\nu_2 = m, \quad (n_1, n_2) \in \mathbb{Z}^2 \backslash \{0, 0\}, \ m \in \mathbb{Z}. \tag{5.7}$$

Without loss of generality, we can set $\gcd(n_1, n_2, m) = 1$ and $m \geq 0$. We refer to such a relation as an $n_1 : n_2 : m$ resonance. Curves of several such resonances are shown in Figure 15.

While resonances are dense in frequency space, those with small order, $|n_1| + |n_2|$, are of particular relevance. For example, the large white region in Figure 15 starting at $b = 0$ and $a \approx -0.75$ corresponds to the $1 : 2 : 1$ resonance. This is also manifested in the broad minimum with $A_{\mathrm{reg}} \approx 0$ in Figure 14. The other prominent minimum near $a \approx -0.5$ is caused by the $2 : 2 : 1$ resonance. In these two cases A_{reg} is reduced in a parameter neighborhood of the resonance curve. For other indicated resonances, i.e., $3 : 2 : 1$, $-1 : 3 : 1$, and $3 : 1 : 1$,

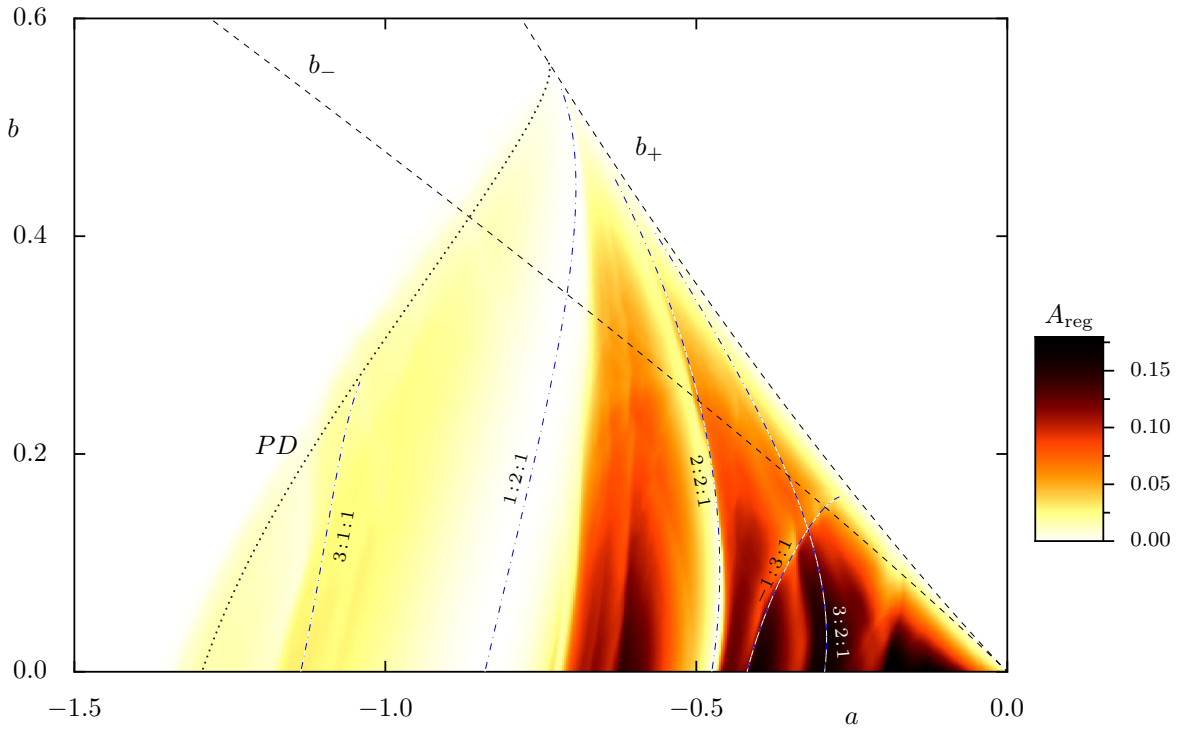

Figure 15. *Area A_{reg} of bounded initial conditions as a function of (a, b) with $c = b$ and $\varepsilon_2 = 1$. The matrix C is defined by $(\alpha, \mu, \delta) = (1, 0.1, 0.5)$, and $\varepsilon_1 = 1$, as in Figure 5(a),(b). The curves $b_\pm$ represent the crossing of the surfaces (3.7) with the plane $c = b$. Thus there are four fixed points when b is below b_- and two when $b_- < b < b_+$. Upon crossing the (dotted) PD curve from right to left, the EE fixed point becomes IE, and A_{reg} rapidly drops to zero. The blue dashed-dotted curves show several resonances (5.7), labeled $n_1 : n_2 : m$, of the EE fixed point.*

the density is only reduced on one side of the bifurcation. In the examples, this happens for smaller a, and sometimes—as for the $3 : 2 : 1$ resonance—it occurs quite some distance away.

Higher-order resonances, $|n_1| + |n_2| \geq 5$, should have less influence on A_{reg}. The results of [21] lead to the expectation that the EE point will remain stable and that for a single resonance the bifurcation creates a pair of invariant 1D tori, one normally hyperbolic and one normally elliptic (at least in the normal form). Further away from the bifurcation of the EE fixed point the geometry is described by bifurcations of families of 1D tori; see [43] and references therein. When the frequency passes through a double resonance so that $\nu_i = p_i/q_i$ are rational, one expects four periodic orbits to be created [21, 60]. According to [21] their stability is either EE + 2 EH + HH or 2 EH + 2 CU; see [42] for an illustration of the geometry in the former case.

Two further examples of A_{reg} are shown in Figure 16 with the same parameters as in Figure 15, except for Figure 16(a) where $c = 5b$, and for Figure 16(b) where the parameter $c = 2$ is fixed. In the latter case the parameter plane no longer intersects the quadfurcation point $(a = b = c = 0)$ so that the curves $b_\pm$ do not intersect at the origin in the figure. In Figure 16(a) the line $b = 0$ corresponds to that in Figure 15 so that the same resonances are still relevant. These now extend to the region $b > 0$, bending strongly to the right. The same overall resonance structure is also visible in Figure 16(b).

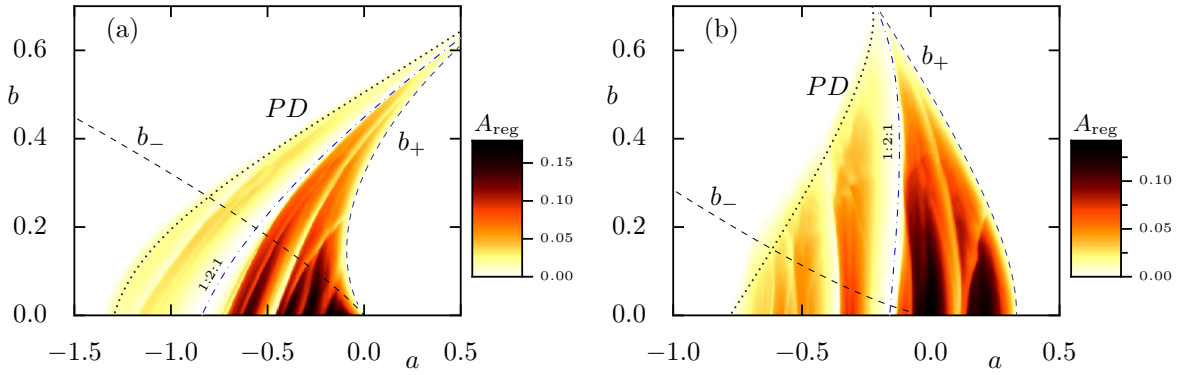

Figure 16. *Area A_{reg} of initial conditions on the* 2D *plane $\eta = C\xi$ inside the box $|\xi_i| \le \kappa/2$ (on a 3000×3000 point grid) that remain within the disk $\|\xi_t\| \le \kappa$ for $t \le 5000$. Variation of (a, b) with* (a) *$c = 5b$ and* (b) *$c = 2$. The remaining parameters are the same as in Figure 15. The curves $b_\pm$ represent the crossing of the surfaces (3.7) with the plane $c = 5b$ or 2, respectively. Thus there are four fixed points when b is below b_- and two when b is between b_- and b_+. To the left of the (dotted) PD line the EE fixed point has become EI.*

6. Coupled Hénon maps.

Since Moser's map (2.2) or, equivalently, (2.9), is the generic, four-dimensional quadratic symplectic map, there must be parameters for which it corresponds to a pair of uncoupled quadratic maps. In this section, we show that this is possible for $\varepsilon_2 = 1$ and special choices of the matrix C, depending on ε_1. The sign ε_1 corresponds to positive and negative Krein signatures. These Hénon maps are uncoupled when $c = 0$. Currently, it is not clear whether there are other possibilities for which the Moser map has uncoupled dynamics with respect to some invariant canonical planes on which the dynamics is conjugate to Hénon maps, and this is left for future study.

Dynamics of a pair of coupled Hénon maps has been studied previously, for example, in [19, 20, 21, 27, 22, 23, 24, 28, 29, 30], particularly in regard to models of storage rings for particle accelerators.

6.1. Decoupled limits: Hénon maps.

To find parameter values for which the Moser map is decoupled, we search for a coordinate transformation that reveals the invariant planes. This transformation should be affine in order to maintain the quadratic form. So that the resulting map is symplectic with the standard Poisson matrix (1.1), and to maintain the momentum-coordinate split for the Hénon form, we start with the linear transformation

$$(\xi, \eta) = S(q, p) = (Aq, \rho A^{-T} p),$$

where A is an invertible matrix and $\rho > 0$. This transformation is symplectic-with-multiplier, $DS^T J DS = \rho J$. In the new coordinates, the map (2.9) becomes

$$\begin{aligned} q' &= q + \hat{C}^{-T}(-p + \hat{C}q + \nabla_q \hat{U}(q)), \\ p' &= \hat{C}q, \end{aligned}$$

where

$$\hat{C} = \frac{1}{\rho} A^T C A, \qquad \hat{U}(q) = \frac{1}{\rho} U(Aq),$$

so that $\nabla_q \hat{U}(q) = \frac{1}{\rho} A^T \nabla_\xi U(Aq)$. In order for the map to be decoupled in the new coordinates, any cross terms in the new potential $\hat{U}$ should be zero. This can be accomplished for (2.10) only if $\varepsilon_2 = 1$, $c = 0$. We can normalize the amplitude of the quadratic terms in the new map by setting $\rho = 1/\sqrt{12}$, choosing

$$A = \rho \begin{pmatrix} 1 & 1 \\ -\sqrt{3} & \sqrt{3} \end{pmatrix}$$

to give

$$\hat{U}(q) = (a - \sqrt{3}b)q_1 + (a + \sqrt{3}b)q_2 + \frac{1}{3}(q_1^3 + q_2^3).$$

The transformation is thus fixed by this choice. So that the resulting map is decoupled, $\hat{C}$ must be diagonal, e.g.,

$$\hat{C} = \begin{pmatrix} \varepsilon_1 & 0 \\ 0 & 1 \end{pmatrix}, \tag{6.1}$$

where $\det C = \det \hat{C} = \varepsilon_1 = \pm 1$. In order for this to be the case, the original C must take one of the following two forms:

$$\varepsilon_1 = 1: \quad C = \begin{pmatrix} \sqrt{3} & 0 \\ 0 & \frac{1}{\sqrt{3}} \end{pmatrix}, \tag{6.2a}$$

$$\varepsilon_1 = -1: \quad C = \begin{pmatrix} 0 & 1 \\ 1 & 0 \end{pmatrix}. \tag{6.2b}$$

Note that one could also replace $\hat{C}$ by $-\hat{C}$ in (6.1), but by the symmetries discussed in section 2.3, this gives nothing new.

With this we get the transformed map

$$\begin{aligned} q_1' &= 2q_1 + \varepsilon_1(-p_1 + a - \sqrt{3}b + q_1^2), \\ p_1' &= \varepsilon_1 q_1, \\ q_2' &= 2q_2 - p_2 + a + \sqrt{3}b + q_2^2, \\ p_2' &= q_2. \end{aligned}$$

This is not quite in the Hénon form (2.1), but a final affine transformation $q \to (\hat{q}_1 - \varepsilon_1, \hat{q}_2 - 1)$ and $p \to \hat{p} - (1, 1)$ brings the map into the form

$$\begin{aligned} \hat{q}_1' &= \varepsilon_1(-\hat{p}_1 + 1 + a - \sqrt{3}b + \hat{q}_1^2), \\ \hat{p}_1' &= \varepsilon_1 \hat{q}_1, \\ \hat{q}_2' &= -\hat{p}_2 + 1 + a + \sqrt{3}b + \hat{q}_2^2, \\ \hat{p}_2' &= \hat{q}_2. \end{aligned} \tag{6.3}$$

Note that after this transformation we obtain, when $\varepsilon_1 = 1$, a pair of uncoupled maps of the Hénon form (2.1). However, when $\varepsilon_1 = -1$, the first canonical pair has the Hénon form

only upon a mirroring transformation, e.g., $(\hat{q}_1, \hat{p}_1) \to (-\hat{q}_1, \hat{p}_1)$; the point is that in the canonical coordinates, the $(\hat{q}_1, \hat{p}_1)$ components "rotate" under the map in the opposite sense from $(\hat{q}_2, \hat{p}_2)$.

The component maps have saddle-center bifurcations along the lines $a = \pm\sqrt{3}b$, creating pairs of fixed points for each component when $a < \pm\sqrt{3}b$, respectively. However, in order for the 4D map to have a fixed point, both components must have fixed points, implying that $a < -\sqrt{3}|b|$. This bifurcation occurs on the same line that appears in Figure 3(a) when $c = 0$.

When the maps are decoupled, and $a < -\sqrt{3}|b|$, the four newly created fixed points have types EE, EH, EH, and HH. In particular, the EE point is located at

$$\varepsilon_1 q_1^* = p_1^* = 1 - \sqrt{\sqrt{3}b - a},$$
$$q_2^* = p_2^* = 1 - \sqrt{-\sqrt{3}b - a}.$$

In the original variables, the fixed points of these maps are given by (3.8) since this corresponds to $c = 0$. The doubly elliptic fixed point remains stable in the rectangle

$$-4 + \sqrt{3}|b| < a < -\sqrt{3}|b|$$

since the individual maps have period-doubling bifurcations at $a = -4 \pm \sqrt{3}b$, respectively.

Recall that for a symplectic map (1.1), with a doubly elliptic fixed point z^*, the quadratic form $q(v) = v^T J Df(z^*) v$ is an invariant of the linearized dynamics. This implies stability when the form q is definite [61, 38]: an EE fixed point cannot cross the $KP = 0$ line in Figure 4 into the CU region. Equivalently, the Krein bifurcation cannot occur if the symmetric matrix

$$\mathcal{Q} = \tfrac{1}{2}[JDf(z^*) - Df^T(z^*)J]$$

is definite. At an elliptic-elliptic point for (6.3), $\mathcal{Q}$ becomes

$$\mathcal{Q} = \left(\begin{array}{cc|cc} \multicolumn{2}{c|}{\multirow{2}{*}{$\hat{C}$}} & -\varepsilon_1 q_1^* & 0 \\ & & 0 & -q_2^* \\ \hline -\varepsilon_1 q_1^* & 0 & \multicolumn{2}{c}{\multirow{2}{*}{$\hat{C}$}} \\ 0 & -q_2^* & & \end{array}\right),$$

where $\hat{C}$ is given in (6.1). When (6.3) has an EE point, $q_i^{*2} < 1$. This implies that $\mathcal{Q}$ is positive definite when $\varepsilon_1 = 1$ but has a pair of negative eigenvalues when $\varepsilon_1 = -1$. Thus, only in the latter case can coupling lead to a Krein bifurcation.

Indeed, we can see this if we reintroduce coupling by allowing $c \neq 0$. The same transformations that lead to (6.3) can be applied if we still take $\varepsilon_2 = 1$ and C to be one of the matrices (6.2). The result is the pair of coupled Hénon maps

$$\begin{aligned} \hat{q}_1' &= \varepsilon_1 \left(-\hat{p}_1 + a_{\mathrm{h}1} + \hat{q}_1^2 + \frac{c}{2\sqrt{3}}(\hat{q}_1 + \hat{q}_2) \right), \\ \hat{p}_1' &= \varepsilon_1 q_1, \\ \hat{q}_2' &= -\hat{p}_2 + a_{\mathrm{h}2} + \hat{q}_2^2 + \frac{c}{2\sqrt{3}}(\hat{q}_1 + \hat{q}_2), \\ \hat{p}_2' &= \hat{q}_2, \end{aligned} \tag{6.4}$$

where

$$a_{h1} = 1 + a - \sqrt{3}b - \frac{\varepsilon_1 + 1}{2\sqrt{3}}c,$$
$$a_{h2} = 1 + a + \sqrt{3}b - \frac{\varepsilon_1 + 1}{2\sqrt{3}}c. \tag{6.5}$$

The stability of the fixed points for this map can be conveniently obtained from the results for the Moser map (2.9). For $\varepsilon_1 = \varepsilon_2 = 1$ and the diagonal matrix in (6.2a), the stability parameters (3.17) become

$$A = 4(1 + \sqrt{3}\xi_1) + \frac{c}{\sqrt{3}},$$
$$B = 6 + \frac{2c}{\sqrt{3}}(1 + \sqrt{3}\xi_1) + 4\sqrt{3}\xi_1(2 + \sqrt{3}\xi_1) - 4\xi_2^2.$$

Since the quadfurcation occurs for $a = b = c = 0$, $\xi_1 = \xi_2 = 0$, it always occurs at the point $(A^Q, B^Q) = (4, 6)$ for this C; indeed, as we showed in section 3.5, this is more generally true for the symmetric case. For this case the Krein parameter (3.19) is always nonpositive,

$$KP = -4\xi_2^2 - c^2/12, \tag{6.6}$$

even when the maps are coupled again by nonzero c. This reflects the fact that for the two 2D uncoupled maps, the elliptic motions in $(\hat{p}_1, \hat{q}_1)$ and $(\hat{p}_2, \hat{q}_2)$ have the same orientation. This is not changed by the coupling when $\varepsilon_1 = +1$, and a CU instability is not possible. This case corresponds to the transition (3.28) with a stability diagram like that shown in Figure 8(b), and neither the EE nor the HH fixed point may turn CU.

For the case when $\varepsilon_2 = 1$ and $\varepsilon_1 = -1$, for the matrix in (6.2b) we similarly obtain

$$A = 4(1 + \xi_2),$$
$$B = 6 - 12\xi_1^2 + 8\xi_2 + 4\xi_2^2 - 2c\xi_1.$$

Now the Krein parameter becomes

$$KP = -2\xi_1(6\xi_1 + c), \tag{6.7}$$

which potentially may have either sign. So when the rotation directions for the two canonical planes are opposed, the coupling terms make a Krein bifurcation possible for nonzero c. Thus the initial quadfurcation may correspond to the transition $\emptyset \to$ EE + HH + 2 EH, as in Figure 8(b), and both the EE and HH might later become CU. In addition, a direct transition to 2 CU + 2 EH is possible, which is analogous to the A-B diagram shown in Figure 8(a) for the fully coupled case.

6.2. Numerical illustration. Let us now illustrate the dynamics near the uncoupled case. Figures 17(a) and (b) show the area, A_{reg}, of bounded orbits for the two cases (6.2) of the matrix C. In these figures, the maps are uncoupled along the line $b = 0$ since we choose $c = 2b$. As in Figures 15 and 16, one observes clear drops of A_{reg} along curves in the (a, b) plane. For

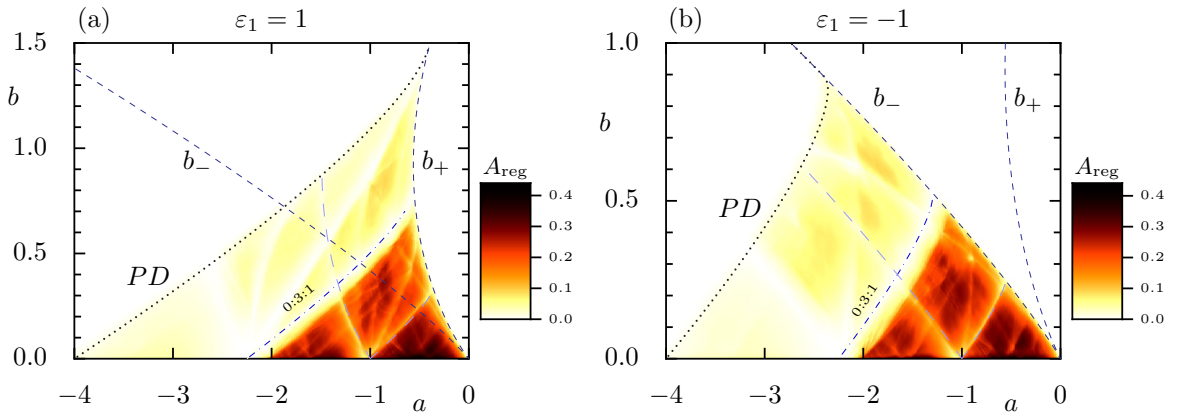

Figure 17. *Area A_{reg} of bounded orbits on the plane $\eta = C\xi$ for the matrices (6.2) with $\varepsilon_2 = 1$, $c = 2b$ and for* (a) $\varepsilon_1 = 1$, *and* (b) $\varepsilon_1 = -1$. *The maps reduce to the uncoupled case only along the axis $b = 0$, since in this case, $c = 0$ as well. The curves $b_\pm$ represent the crossing of the surfaces (3.7) with the plane $c = 2b$. Thus there are four fixed points when b is below b_- and two when b is between b_- and b_+. For both examples, to the left of the (dotted) PD line the EE fixed point becomes EI. The dashed-dotted line shows the $0:3:1$ resonance near the location where there is a strong decrease in A_{reg}. The long-dashed (light blue) lines show the $4:0:1$ resonance (left branch) and the $0:4:1$ resonance (right branch) that emanate from $(a, b) = (-1, 0)$ corresponding to the quadrupling bifurcation in the uncoupled case.*

the uncoupled case, when $b = 0$, the two plots in Figure 17 agree because the individual 2D maps in (6.4) have the same parameters $a_{\rm h1} = a_{\rm h2}$. In both panels, the b_- line corresponds to a saddle-center bifurcation, but in Figure 17(a) two fixed points with stabilities EH and HH disappear upon reaching b_- from below; thus the decrease in the number of fixed points has no significant influence on the size of $A_{\rm reg}$. In contrast, for Figure 17(b) the fixed points with stabilities EE and EH disappear upon reaching b_- from below, so that only the EH and HH fixed points are left in the region between b_- and b_+, and $A_{\rm reg}$ decreases abruptly. As $\varepsilon_1 = 1$ in Figure 17(a), none of the fixed points can become CU. For $\varepsilon_1 = -1$, as in Figure 17(b), the HH fixed point becomes CU when a is sufficiently negative, but again this does not significantly influence $A_{\rm reg}$.

In both panels of Figure 17 the $0:3:1$ resonance curve of the EE fixed point leads to a strong reduction in bounded area as a decreases through the resonance. There is also a strong reduction for both cases in $A_{\rm reg}$ along two lines that meet in $(a, b) = (-1, 0)$. At this parameter value the uncoupled Hénon maps have a fourth-order resonance; see, e.g., [59] for a detailed study of the 2D case. The right line corresponds to the $0:4:1$ resonance, and the left to the $4:0:1$ resonance. For both resonances the reduction happens to the left of the lines, i.e., for smaller values of a. This corresponds to the direction in which the quadrupling bifurcation creates new elliptic and hyperbolic fixed points and 1D tori.

Figure 18 shows a 3D phase space slice plot and an escape time plot in the (ξ_1, ξ_2)-plane for $(a, b, c) = (-0.3, 0.1, 0.2)$ and $\varepsilon_1 = 1$. The elliptic-elliptic fixed point is surrounded by a region of predominantly regular motion as seen by the white region of nonescaping orbits (within 10^4 iterations). Corresponding regular 2D tori are shown as black curves in the slice. Some of these are secondary tori around periodic orbits and appear as sequences of disjoint loops

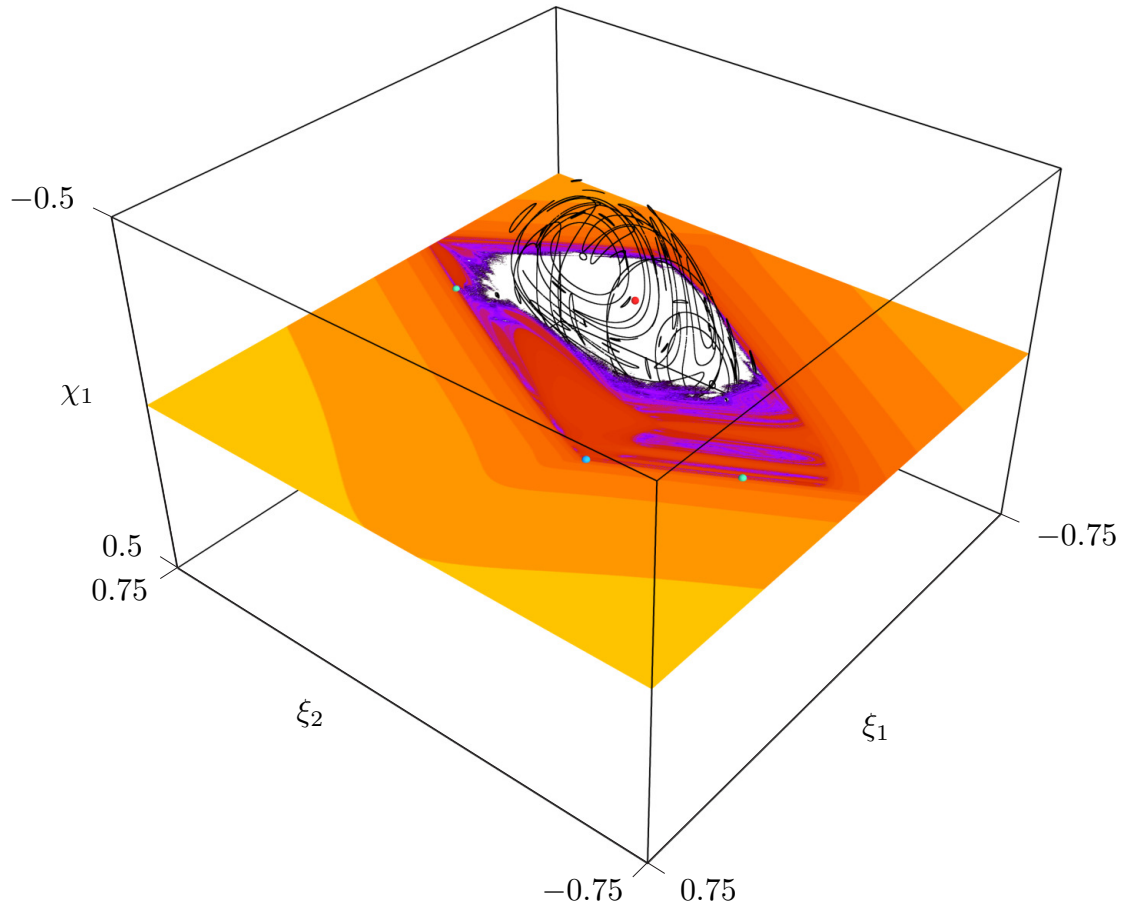

Figure 18. 3D *phase space slice and corresponding escape time plot in the* $\eta = C\xi$ *plane for the diagonal matrix* C *of* (6.2a) *with* $\varepsilon_1 = 1$ *and* $(a, b, c) = (-0.3, 0.1, 0.2)$. *Shown are several selected regular tori (black lines) near the "outer edge" of the "regular region" surrounding the EE fixed point. Each torus is represented by* 10^4 *points in the slice with* $\epsilon = 10^{-6}$. *The four fixed points are shown as small spheres: EE (red), 2 EH (green), and HH (blue). The coloring of the escape times is the same as in Figure* 13. *For a rotating view see* M126866_04.mp4 [local/web 14.3MB].

in the 3D phase space slice. The HH fixed point and the two EH fixed points approximately limit the region in which the regular orbits and orbits with longer escape times are contained.

7. Summary and outlook. In this paper we have studied some of the dynamics of Moser's 4D quadratic, symplectic maps, which have normal form (2.9) with six parameters $a, b, c, \alpha, \delta, \mu$ and two discrete parameters $\varepsilon_1, \varepsilon_2$. We showed that there is a codimension-three submanifold in parameter space for which Moser's map has a single fixed point with a pair of unit eigenvalues. Bifurcations that occur on this submanifold correspond to creation and destruction of up to four fixed points, the maximum possible number for the map (except for one singular case). Along paths in parameter space that pass through this singularity, it is possible for four fixed points to be created from none—a quadfurcation. For other paths, two fixed points may be

created, or they collide and emerge as two or four; recall Figure 3 and Table 1. Intuitively, the simplest case corresponds to a pair of uncoupled 2D Hénon maps, where a quadfurcation corresponds to choosing parameters so that the maps have simultaneous, colocated saddle-center bifurcations.

When a fixed point has four distinct eigenvalues on the unit circle (i.e., has type "EE"), then it is linearly stable, and according to KAM theory, it is generically surrounded by a Cantor family of invariant two-tori. We have seen that it is possible for one or two EE fixed points to emerge from the quadfurcation. The remaining two fixed points have at least one hyperbolic pair of eigenvalues. For the case of uncoupled Hénon maps, the four fixed points correspond to the cross-products of the saddles and centers of the two area-preserving maps, giving rise to a single EE fixed point, two EH points, and one HH point. This scenario persists when coupling is added and, as we will show in a future paper, can describe the creation of accelerator modes in a 4D standard map near zero coupling. However, this scenario is rather special from the point view of Moser's map, where more typically, one has the creation of two EE and two EH fixed points, unless the matrix C is symmetric.

For symmetric C, where the map is reversible, the quadfurcation has the special feature that the fixed points are born with four unit eigenvalues. This allows, for example, the direct creation of complex unstable, CU fixed points. It is also of interest that when C is symmetric, the limiting form of Moser's map near the quadfurcation is a natural Hamiltonian system (3.32). It is still an open question whether the map is reversible *only* when C is symmetric

We showed in Theorem 1 that, when $\varepsilon_2 \neq 0$, there is a ball that contains all bounded orbits. We observe that orbits that remain bounded are typically associated with the EE fixed points. The computations suggest that the center-stable manifolds of the EH points are likely candidates for partial barriers that delineate the boundary of the region of orbits that have long escape times. In a future paper, we hope to compute these manifolds to better understand the geometry of the barriers.

There are several other interesting questions left for future studies. For the 2D case, where the Hénon map provides the universal form for any quadratic area-preserving map, the algebraic decay of the survival probability for the escape from a neighborhood of the regular region is well established and understood in terms of partial barriers and is approximately described by Markov models. While for higher-dimensional maps such power-law stickiness is numerically well established, the mechanism for this is still not understood. Moser's map is the prototypical example for the study of the stickiness of a regular region in 4D. Of course, in this context, Arnold diffusion also will be important.

Finally, it would be of interest to study similar bifurcations for polynomial maps of higher degree; for example, the cubic case can be written in the Moser form as a composition of affine maps with a symplectic shear [33], and, of course, one can wonder what other exotic local bifurcations may happen in symplectic maps of even higher dimension.

Acknowledgments. We would like to thank Robert Easton, Roland Ketzmerick, Rafael de la Llave, and Martin Richter for useful discussions. The visualizations of the 3D phase space slices were created using Mayavi [62].

REFERENCES

[1] P. M. Cincotta, *Arnold diffusion: An overview through dynamical astronomy*, New Astron. Rev., 46 (2002), pp. 13–39, https://doi.org/10.1016/S1387-6473(01)00153-1.

[2] G. Contopoulos and M. Harsoula, *3D chaotic diffusion in barred spiral galaxies*, Mon. Not. R. Astron. Soc., 436 (2013), pp. 1201–1214, https://doi.org/10.1093/mnras/stt1640.

[3] S. Gekle, J. Main, T. Bartsch, and T. Uzer, *Extracting multidimensional phase space topology from periodic orbits*, Phys. Rev. Lett., 97 (2006), 104101, http://link.aps.org/doi/10.1103/PhysRevLett.97.104101.

[4] R. Paškauskas, C. Chandre, and T. Uzer, *Dynamical bottlenecks to intramolecular energy flow*, Phys. Rev. Lett., 100 (2008), 083001, https://doi.org/10.1103/PhysRevLett.100.083001.

[5] J. D. Meiss, *Differential Dynamical Systems*, rev. ed., Math. Model. Comput. 22, SIAM, Philadelphia, 2017, https://doi.org/10.1137/1.9781611974645.

[6] R. I. McLachlan and G. R. W. Quispel, *Geometric integrators for ODEs*, J. Phys. A, 39 (2006), pp. 5251–5285, https://doi.org/10.1088/0305-4470/39/19/S01.

[7] E. Forest, *Geometric integration for particle accelerators*, J. Phys. A, 39 (2006), pp. 5321–5377, http://iopscience.iop.org/0305-4470/39/19/S03.

[8] P. Gaspard and S. A. Rice, *Hamiltonian mapping models of molecular fragmentation*, J. Phys. Chem., 93 (1989), pp. 6947–6957, https://doi.org/10.1021/j100356a014.

[9] R. E. Gillilan and G. S. Ezra, *Transport and turnstiles in multidimensional Hamiltonian mappings for unimolecular fragmentation: Application to van der Waals predissociation*, J. Chem. Phys., 94 (1991), pp. 2648–2668, https://doi.org/10.1063/1.459840.

[10] R. L. Warnock and R. D. Ruth, *Long-term bounds on nonlinear Hamiltonian motion*, Phys. D, 56 (1992), pp. 188–215, https://doi.org/10.1016/0167-2789(92)90024-H.

[11] H. S. Dumas and J. Laskar, *Global dynamics and long-time stability in Hamiltonian systems via numerical frequency analysis*, Phys. Rev. Lett., 70 (1993), pp. 2975–2979, https://doi.org/10.1103/PhysRevLett.70.2975.

[12] J. E. Howard, A. J. Lichtenberg, M. A. Lieberman, and R. H. Cohen, *Four-dimensional mapping model for two-frequency electron cyclotron resonance heating*, Phys. D, 20 (1986), pp. 259–284, https://doi.org/10.1016/0167-2789(86)90033-3.

[13] G. Casati, I. Guarneri, and D. L. Shepelyansky, *Two-frequency excitation of hydrogen atom*, Chaos Solitons Fractals, 1 (1991), pp. 131–135, https://doi.org/10.1016/0960-0779(91)90003-R.

[14] J. Wisdom and M. Holman, *Symplectic maps for the N-body problem*, Astron. J., 102 (1991), pp. 1528–1538, https://doi.org/10.1086/115978.

[15] M. Hénon, *Numerical study of quadratic area-preserving mappings*, Quart. Appl. Math., 27 (1969), pp. 291–312, https://doi.org/10.1090/qam/253513.

[16] M. Hénon, *A two-dimensional mapping with a strange attractor*, Comm. Math. Phys., 50 (1976), pp. 69–77, https://doi.org/10.1007/BF01608556.

[17] C. F. F. Karney, A. B. Rechester, and R. B. White, *Effect of noise on the standard mapping*, Phys. D, 4 (1982), pp. 425–438, https://doi.org/10.1016/0167-2789(82)90045-8.

[18] D. Turaev, *Polynomial approximations of symplectic dynamics and richness of chaos in non-hyperbolic area-preserving maps*, Nonlinearity, 16 (2003), pp. 123–135, https://doi.org/10.1088/0951-7715/16/1/308.

[19] J.-m. Mao, *Standard form of four-dimensional symplectic quadratic maps*, Phys. Rev. A, 38 (1988), pp. 525–526, http://link.aps.org/doi/10.1103/PhysRevA.38.525.

[20] M. Ding, T. Bountis, and E. Ott, *Algebraic escape in higher dimensional Hamiltonian systems*, Phys. Lett. A, 151 (1990), pp. 395–400, https://doi.org/10.1016/0375-9601(90)90910-G.

[21] E. Todesco, *Analysis of resonant structure of four-dimensional symplectic mappings, using normal forms*, Phys. Rev. E, 50 (1994), pp. R4298–R4301, https://doi.org/10.1103/PhysRevE.50.R4298.

[22] E. Todesco, *Local analysis of formal stability and existence of fixed points in 4d symplectic mappings*, Phys. D, 95 (1996), pp. 1–12, https://doi.org/10.1016/0167-2789(95)00290-1.

[23] M. Gemmi and E. Todesco, *Stability and geometry of third-order resonances in four-dimensional symplectic mappings*, Celestial Mech. Dynam. Astron., 67 (1997), pp. 181–204, https://doi.org/10.1023/A:1008288826727.

[24] M. N. Vrahatis, T. C. Bountis, and M. Kollmann, *Periodic orbits and invariant surfaces of 4D nonlinear mappings*, Int. J. Bifur. Chaos, 6 (1996), pp. 1425–1437, https://doi.org/10.1142/s0218127496000849.

[25] H. R. Dullin and J. D. Meiss, *Twist singularities for symplectic maps*, Chaos, 13 (2003), pp. 1–16, https://doi.org/10.1063/1.1529450.

[26] S. V. Gonchenko, D. V. Turaev, and L. P. Shilnikov, *Existence of infinitely many elliptic periodic orbits in four-dimensional symplectic maps with a homoclinic tangency*, Proc. Steklov. Inst. Math., 244 (2004), pp. 106–131.

[27] T. Bountis and M. Kollmann, *Diffusion rates in a 4-dimensional mapping model of accelerator dynamics*, Phys. D, 71 (1994), pp. 122–131, https://doi.org/10.1016/0167-2789(94)90185-6.

[28] M. N. Vrahatis, H. Isliker, and T. C. Bountis, *Structure and breakdown of invariant tori in a 4-D mapping model of accelerator dynamics*, Int. J. Bifur. Chaos, 7 (1997), pp. 2707–2722, https://doi.org/10.1142/S0218127497001825.

[29] M. Giovannozzi, W. Scandale, and E. Todesco, *Dynamic aperture extrapolation in the presence of tune modulation*, Phys. Rev. E, 57 (1998), pp. 3432–3443, https://link.aps.org/doi/10.1103/PhysRevE.57.3432.

[30] T. Bountis and Ch. Skokos, *Application of the SALI chaos detection method to accelerator mappings*, Nuclear Inst. Methods Phys. Res. Sec. A, 561 (2006), pp. 173–179, https://doi.org/10.1016/j.nima.2006.01.009.

[31] J. K. Moser, *On quadratic symplectic mappings*, Math. Z., 216 (1994), pp. 417–430, https://doi.org/10.1007/BF02572331.

[32] H. Bass, E. H. Connell, and D. Wright, *The Jacobian conjecture: Reduction of degree and formal expansion of the inverse*, Bull. Amer. Math. Soc., 7 (1982), pp. 287–330, https://doi.org/10.1090/S0273-0979-1982-15032-7.

[33] H. Koch and H. Lomelí, *On Hamiltonian flows whose orbits are straight lines*, Discrete Contin. Dyn. Syst. Ser. A, 34 (2014), pp. 2091–2104, https://doi.org/10.3934/dcds.2014.34.2091.

[34] S. H. Strogatz, *Nonlinear Dynamics and Chaos: With Applications in Physics, Biology, Chemistry, and Engineering*, 2nd ed., Studies in Nonlinearity, Westview Press, Boulder, CO, 2015.

[35] J. D. Meiss, *Thirty years of turnstiles and transport*, Chaos, 25 (2015), 097602, https://doi.org/10.1063/1.4915831.

[36] H.-t. Kook and J. D. Meiss, *Periodic orbits for reversible, symplectic mappings*, Phys. D, 35 (1989), pp. 65–86, https://doi.org/10.1016/0167-2789(89)90096-1.

[37] R. Broucke, *Stability of periodic orbits in the elliptic, restricted three-body problem*, AIAA J., 7 (1969), pp. 1003–1009, https://doi.org/10.2514/3.5267.

[38] J. E. Howard and R. S. MacKay, *Linear stability of symplectic maps*, J. Math. Phys., 28 (1987), pp. 1036–1051, https://doi.org/10.1063/1.527544.

[39] M. G. Kreĭn, *Topics in Differential and Integral Equations and Operator Theory*, I. Gohberg, ed., translated from the Russian by A. Iacob, Oper. Theory Adv. Appl. 7, Birkhäuser Verlag, Basel, 1983.

[40] J. W. S. Lamb and J. A. G. Roberts, *Time-reversal symmetry in dynamical systems: A survey*, Phys. D, 112 (1998), pp. 1–39, https://doi.org/10.1016/S0167-2789(97)00199-1.

[41] M. Richter, S. Lange, A. Bäcker, and R. Ketzmerick, *Visualization and comparison of classical structures and quantum states of four-dimensional maps*, Phys. Rev. E, 89 (2014), 022902, http://link.aps.org/doi/10.1103/PhysRevE.89.022902.

[42] S. Lange, M. Richter, F. Onken, A. Bäcker, and R. Ketzmerick, *Global structure of regular tori in a generic 4D symplectic map*, Chaos, 24 (2014), 024409, https://doi.org/10.1063/1.4882163.

[43] F. Onken, S. Lange, R. Ketzmerick, and A. Bäcker, *Bifurcations of families of 1D-tori in 4D symplectic maps*, Chaos, 26 (2016), 063124, https://doi.org/10.1063/1.4954024.

[44] S. Lange, A. Bäcker, and R. Ketzmerick, *What is the mechanism of power-law distributed Poincaré recurrences in higher-dimensional systems?*, Europhys. Lett., 116 (2016), 30002, https://doi.org/10.1209/0295-5075/116/30002.

[45] S. Anastassiou, T. Bountis, and A. Bäcker, *Homoclinic points of 2D and 4D maps via the parametrization method*, Nonlinearity, 30 (2017), pp. 3799–3820, https://doi.org/10.1088/1361-6544/aa7e9b.

[46] M. Firmbach, S. Lange, R. Ketzmerick, and A. Bäcker, *Three-dimensional billiards: Visualization of regular structures and trapping of chaotic trajectories*, Phys. Rev. E, 98 (2018), 022214, https://doi.org/10.1103/PhysRevE.98.022214, 2018.

[47] J. K. Moser, *On invariant curves of area-preserving mappings of an annulus*, Nachr. Akad. Wiss. Göttingen, Math.-Phys. Kl. II, 1962 (1962), pp. 1–20.
[48] A. Delshams and P. Gutiérrez, *Estimates on invariant tori near an elliptic equilibrium point of a Hamiltonian system*, J. Differential Equations, 131 (1996), pp. 277–303, https://doi.org/10.1006/jdeq.1996.0165.
[49] L. H. Eliasson, B. Fayad, and R. Krikorian, *KAM-tori near an analytic elliptic fixed point*, Regul. Chaotic Dyn., 18 (2013), pp. 801–831, https://doi.org/10.1134/S1560354713060154.
[50] J. Laskar, *Frequency analysis for multi-dimensional systems: Global dynamics and diffusion*, Phys. D, 67 (1993), pp. 257–281, https://doi.org/10.1016/0167-2789(93)90210-R.
[51] R. Bartolini, A. Bazzani, M. Giovannozzi, W. Scandale, and E. Todesco, *Tune evaluation in simulations and experiments*, Part. Accel., 52 (1996), pp. 147–177, https://cdsweb.cern.ch/record/292773.
[52] P. A. Patsis and L. Zachilas, *Using color and rotation for visualizing four-dimensional Poincaré cross-sections: With applications to the orbital behavior of a three-dimensional Hamiltonian system*, Int. J. Bifur. Chaos, 4 (1994), pp. 1399–1424, https://doi.org/10.1142/S021812749400112X.
[53] V. I. Arnol'd, *Instability of dynamical systems with several degrees of freedom*, Sov. Math. Dokl., 5 (1964), pp. 581–585.
[54] B. V. Chirikov, *A universal instability of many-dimensional oscillator systems*, Phys. Rep., 52 (1979), pp. 263-379, https://doi.org/10.1016/0370-1573(79)90023-1.
[55] P. Lochak, *Arnold diffusion; a compendium of remarks and questions*, in Hamiltonian Systems with Three or More Degrees of Freedom (S'Agaró, Spain, 1995), C. Simó, ed., Springer, Dordrecht, 1999, pp. 168–183, https://doi.org/10.1007/978-94-011-4673-9_15.
[56] H. S. Dumas, *The KAM Story: A Friendly Introduction to the Content, History, and Significance of Classical Kolmogorov–Arnold–Moser Theory*, World Scientific, Singapore, 2014.
[57] C. F. F. Karney, A. B. Rechester, and R. B. White, *Effect of noise on the standard mapping*, Phys. D, 4 (1982), pp. 425–438, https://doi.org/10.1016/0167-2789(82)90045-8.
[58] J. D. Meiss, *Average exit time for volume-preserving maps*, Chaos, 7 (1997), pp. 139–147, https://doi.org/10.1063/1.166245.
[59] C. Simó and A. Vieiro, *Resonant zones, inner and outer splittings in generic and low order resonances of area preserving maps*, Nonlinearity, 22 (2009), pp. 1191–1245, http://iopscience.iop.org/0951-7715/22/5/012.
[60] V. Gelfreich, C. Simó, and A. Vieiro, *Dynamics of 4D symplectic maps near a double resonance*, Phys. D, 243 (2013), pp. 92–110, https://doi.org/10.1016/j.physd.2012.10.001.
[61] V. I. Arnold and A. Avez, *Ergodic Problems of Classical Mechanics*, Benjamin, New York, 1968.
[62] P. Ramachandran and G. Varoquaux, *Mayavi: 3D visualization of scientific data*, Comput. Sci. Eng., 13 (2011), pp. 40–51, https://doi.org/10.1109/MCSE.2011.35.